

AD-A040 658

STANFORD RESEARCH INST MENLO PARK CALIF

F/G 11/6

CHARACTERIZATION OF THE DYNAMIC BEHAVIOR OF POROUS SOLIDS. VOLU--ETC(U)

MAR 76 J T ROSENBERG, M J GINSBERG

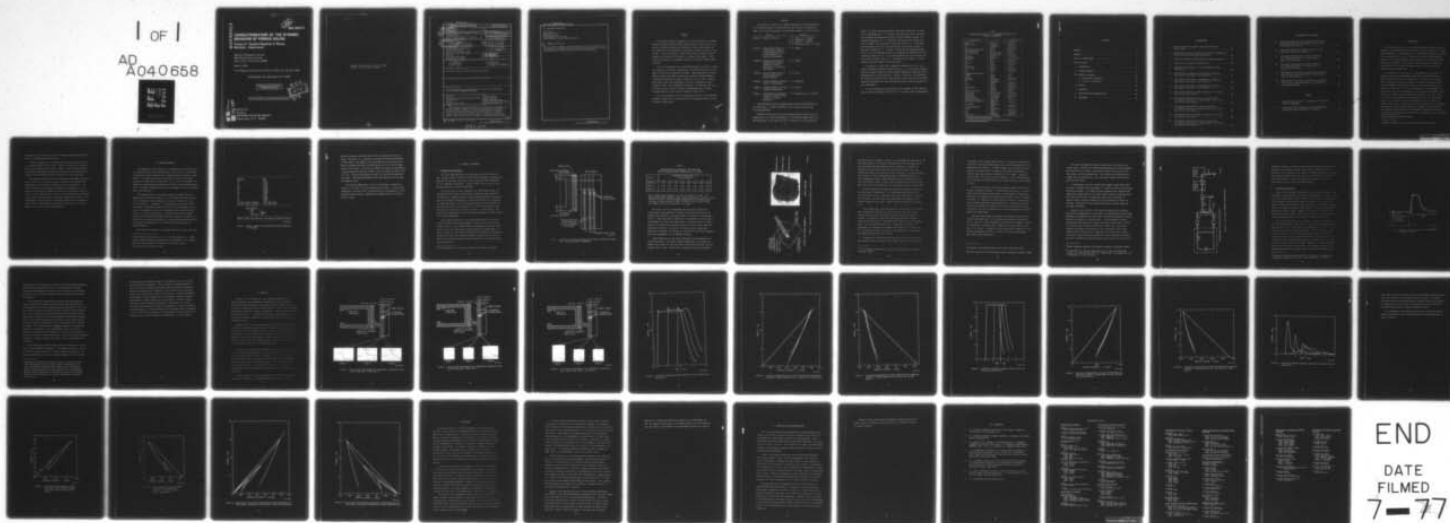
DNA001-74-C-0150

UNCLASSIFIED

DNA-3961F-5

NL

1 OF 1
AD
A040658



END

DATE

FILMED

7-77

AD A 040658

12 B.S.

DNA 3961F-5

CHARACTERIZATION OF THE DYNAMIC BEHAVIOR OF POROUS SOLIDS

Volume 5 - Dynamic Response of Porous
Beryllium - Experiments

Stanford Research Institute
333 Ravenswood Avenue
Menlo Park, California 94025

March 1976

Final Report for Period 14 January 1974 - 31 January 1976

CONTRACT No. DNA 001-74-C-0150

APPROVED FOR PUBLIC RELEASE;
DISTRIBUTION UNLIMITED.

DDC
JUN 16 1977
RECEIVED
C

THIS WORK SPONSORED BY THE DEFENSE NUCLEAR AGENCY
UNDER RDT&E RMSS CODE B342076464 N99QAXAC30840 H2590D.

AD No.
DDC FILE COPY

Prepared for

Director

DEFENSE NUCLEAR AGENCY

Washington, D. C. 20305

Destroy this report when it is no longer
needed. Do not return to sender.



UNCLASSIFIED

SECURITY CLASSIFICATION OF THIS PAGE (When Data Entered)

REPORT DOCUMENTATION PAGE		READ INSTRUCTIONS BEFORE COMPLETING FORM
1. REPORT NUMBER DNA 3961F-5	2. GOVT ACCESSION NO.	3. RECIPIENT'S CATALOG NUMBER
4. TITLE (and Subtitle) CHARACTERIZATION OF THE DYNAMIC BEHAVIOR OF POROUS SOLIDS. Volume 5. Dynamic Response of Porous Beryllium—Experiments.	5. TYPE OF REPORT & PERIOD COVERED Final Report for Period 14 Jan 74—31 Jan 76.	6. PERFORMING ORG. REPORT NUMBER SRI Project PYU-3163
7. AUTHOR(s) J. T. Rosenberg, Author M. J. Ginsberg, Project Leader D. R. Curran, Project Supervisor	8. CONTRACT OR GRANT NUMBER(s) DNA 001-74-C-0150	
9. PERFORMING ORGANIZATION NAME AND ADDRESS Stanford Research Institute 333 Ravenswood Avenue Menlo Park, California 94025	10. PROGRAM ELEMENT, PROJECT, TASK AREA & WORK UNIT NUMBERS Subtask N99QAXAC308-40	
11. CONTROLLING OFFICE NAME AND ADDRESS Director Defense Nuclear Agency Washington, D.C. 20305	12. REPORT DATE Mar 76	
13. NUMBER OF PAGES 54	14. MONITORING AGENCY NAME & ADDRESS (if different from Controlling Office) 1249p.	15. SECURITY CLASS (of this report) UNCLASSIFIED
15a. DECLASSIFICATION/DOWNGRADING SCHEDULE		
16. DISTRIBUTION STATEMENT (of this Report) Approved for public release; distribution unlimited.		
17. DISTRIBUTION STATEMENT (of the abstract entered in Block 20, if different from Report)		
18. SUPPLEMENTARY NOTES This work sponsored by the Defense Nuclear Agency under RDT&E RMSS Code B342076464 N99QAXAC30840 H2590D.		
19. KEY WORDS (Continue on reverse side if necessary and identify by block number) Beryllium In-Material Gages Plasma Sprayed Distended Beryllium (PSDB) Lagrange Analysis Porous Materials Stress-Volume Histories Gas Gun Dynamic Compression and Release Ytterbium Stress Gages Irreversible Compaction		
20. ABSTRACT (Continue on reverse side if necessary and identify by block number) Planar-impact gas gun experiments were performed to investigate the dynamic mechanical response of nonsintered plasma-sprayed distended beryllium (PSDB) shock-loaded to stress levels below full compaction. Stress-time profiles were obtained at several depths in each PSDB target, using in-material ytterbium gages. A Lagrangian analysis was applied to the stress histories to produce dynamic stress-volume paths.		

DD FORM 1473 1 JAN 73 EDITION OF 1 NOV 65 IS OBSOLETE

UNCLASSIFIED

SECURITY CLASSIFICATION OF THIS PAGE (When Data Entered)

332 500

LB

UNCLASSIFIED

SECURITY CLASSIFICATION OF THIS PAGE(When Data Entered)

19. KEY WORDS (Continued)

Crush Curve
Nonattenuating Flow
Attenuating Flow
Time Dependent Pore Collapse
Stress Overshoot, Decay, and Recompression

↓ 20. ABSTRACT (Continued)

PSDB was shown to undergo irreversible compaction at stress levels as low as 4 kbar, and in several profiles an unexpected stress overshoot, decay, and recompression history was observed after initial compression. ↗

UNCLASSIFIED

SECURITY CLASSIFICATION OF THIS PAGE(When Data Entered)

SUMMARY

The dynamic mechanical compression and release behavior of plasma-sprayed distended beryllium (PSDB) impact-loaded to less than full compaction has been experimentally determined. Three planar impact gas gun experiments were performed at peak impact stresses of between 4 and 16 kbar. In each experiment, stress profiles were recorded at several depths in the target with in-material ytterbium stress gages. These profiles were used in a Lagrangian analysis to calculate stress-volume histories.

Two of the experiments were nonattenuating shots in which a constant peak stress, 4 and 16 kbar, respectively, was achieved and held at each gage position before subsequent unloading. These experiments provided dynamic loading and release trajectories showing that PSDB undergoes irreversible compaction at impact stresses as low as 4 kbar. Several gage records from these experiments also show an unexpected stress-overshoot, decay, and recompression structure. We speculate that this structure may be a result of complex time-dependent pore collapse, although additional work would be required to verify this.

The third experiment was an attenuating flow shot. This experiment provided a useful set of stress histories for checking predictive capabilities of PSDB models.

DISTRIBUTION/AVAILABILITY CODES	
Dist.	AVAIL. FOR SPECIAL
A	

PREFACE

This report is Volume 5 in a seven-volume series on Characterization of the Dynamic Behavior of Porous Solids, DNA Contract No. DNA001-74-C-0150. The titles and authors of the individual reports in the series are:

Title	Author(s)
Volume 1. Summary of Results	D. R. Curran, R. E. Tokheim, M. J. Ginsberg, L. Seaman, A. B. Lutze, D. C. Erlich, J. T. Rosenberg, and D. A. Shockey
Volume 2. Computational Models for Predicting the Dynamic Stress Response of Some Porous Ceramics in a Radiation Environment	R. E. Tokheim
Volume 3. Computational Model for Predicting the Dynamic Response of Porous Beryllium in a Radiation Environment	R. E. Tokheim
Volume 4. Electron Beam Studies of Porous Beryllium and Porous Ceramics	A. B. Lutze
Volume 5. Dynamic Response of Porous Beryllium--Experiments	J. T. Rosenberg
Volume 6. Dynamic Response of Porous Ceramics--Experiments	D. C. Erlich
Volume 7. Microstructural Characterization of Several Porous Ceramics and Porous Beryllium	D. A. Shockey and J. P. Wilhelm

The Contracting Officer's Representative during the performance of this work was D. J. Kohler (DNA/SPAS), and the Project Monitor was K. Smith (AFWL/DYV).

Because of the toxicity of the beryllium specimen material and the complexity of the required experiments, the successful completion of the work described in this report was due in large part to the exceptional

support the author received from both inside and outside SRI. I would like to acknowledge Mr. C. H. Anderson, SRI Health and Safety Services, for developing and demonstrating safe beryllium handling, firing, and disposal procedures; Mr. A. J. Bartlett, SRI gas gun site leader, for safely, rapidly, and successfully firing the shots; Mr. J. H. Hannigan, SRI engineering assistant, for constructing the beryllium targets to exacting standards; Mr. D. F. Walter, SRI electronics engineering associate, for his thoroughness and care in designing and operating the data recording systems; Mrs. B. Y. Lew, SRI mathematician, for her usual fine job of data analysis; and Dr. M. J. Ginsberg, Project Leader, for much helpful advice and support during this effort.

In addition, I would like to express my appreciation to Mr. W. M. Isbell of Lawrence Livermore Laboratory and Mr. A. O. Burford of Lockheed Missile and Space Company for their helpful suggestions regarding dynamic experiments with porous beryllium. Finally, I would like to acknowledge Mr. Bob Baird, Linde Division, Union Carbide Corporation who was extremely helpful and responsive in manufacturing high quality specimen material to our requirements.

For the convenience of the reader we have included on the following page a table of conversion factors for U.S. to metric units of measurement.

Table
CONVERSION FACTORS FOR U.S. CUSTOMARY TO METRIC (SI)
UNITS OF MEASUREMENT

To Convert From	To	Multiply By
angstrom	meters (m)	1.000 000 X E -10
atmosphere (normal)	kilo pascal (kPa)	1.013 25 X E +2
bar	kilo pascal (kPa)	1.000 000 X E +2
barn	meter ² (m ²)	1.000 000 X E -28
British thermal unit (thermochemical)	joule (J)	1.054 350 X E +3
calorie (thermochemical)	joule (J)	4.184 000
cal (thermochemical)/cm ²	mega joule/m ² (MJ/m ²)	4.184 000 X E -2
curie	*giga becquerel (GBq)	3.700 000 X E +1
degree (angle)	radian (rad)	1.745 329 X E -2
degree Fahrenheit	degree kelvin (K)	$t_K = (t_F + 459.67)/1.8$
electron volt	joule (J)	1.602 19 X E -19
erg	joule (J)	1.000 000 X E -7
erg/second	watt (W)	1.000 000 X E -7
foot	meter (m)	3.048 000 X E -1
foot-pound-force	joule (J)	1.355 818
gallon (U. S. liquid)	meter ³ (m ³)	3.785 412 X E -3
inch	meter (m)	2.540 000 X E -2
jerk	joule (J)	1.000 000 X E +9
joule/kilogram (J/kg) (radiation dose absorbed)	Gray (Gy)	1.000 000
kilotons	terajoules	4.183
kip (1000 lbf)	newton (N)	4.448 222 X E +3
kip/inch ² (ksi)	kilo pascal (kPa)	6.894 757 X E +3
ktap	newton-second/m ² (N-s/m ²)	1.000 000 X E +2
micron	meter (m)	1.000 000 X E -6
mil	meter (m)	2.540 000 X E -5
mile (international)	meter (m)	1.609 344 X E +3
ounce	kilogram (kg)	2.834 952 X E -2
pound-force (lbs avoirdupois)	newton (N)	4.448 222
pound-force inch	newton-meter (N·m)	1.129 848 X E -1
pound-force/inch	newton/meter (N/m)	1.751 268 X E +2
pound-force/foot ²	kilo pascal (kPa)	4.788 026 X E -2
pound-force/inch ² (psi)	kilo pascal (kPa)	6.894 757
pound-mass (lbm avoirdupois)	kilogram (kg)	4.535 924 X E -1
pound-mass-foot ² (moment of inertia)	kilogram-meter ² (kg·m ²)	4.214 011 X E -2
pound-mass/foot ³	kilogram/meter ³ (kg/m ³)	1.601 846 X E +1
rad (radiation dose absorbed)	**Gray (Gy)	1.000 000 X E -2
roentgen	coulomb/kilogram (C/kg)	2.579 760 X E -4
shake	second (s)	1.000 000 X E -8
slug	kilogram (kg)	1.459 390 X E +1
torr (mm Hg, 0° C)	kilo pascal (kPa)	1.333 22 X E -1

*The becquerel (Bq) is the SI unit of radioactivity; 1 Bq = 1 event/s.

**The Gray (Gy) is the SI unit of absorbed radiation.

A more complete listing of conversions may be found in "Metric Practice Guide E 380-74," American Society for Testing and Materials.

CONTENTS

SUMMARY	1
PREFACE	2
LIST OF ILLUSTRATIONS	6
LIST OF TABLES	7
I INTRODUCTION	9
II SPECIMEN MATERIAL	11
III METHOD OF APPROACH	14
A. Experimental Techniques	14
B. Analytical Techniques	22
IV RESULTS	26
V DISCUSSION	42
VI CONCLUSIONS AND RECOMMENDATIONS	45
VII REFERENCES	47

ILLUSTRATIONS

1.	Quality Control Test Report, Beryllium Powder KBI Lot No. 2084	12
2.	Schematic Side View of Projectile and Target Configuration Used in All Three PSDB Impact Experiments	15
3.	Gage Plane Schematic and Photograph of Completed Target . .	17
4.	Gage Circuit, Schematic Representation	21
5.	Schematic Representation of a Piezoresistant Stress Gage Record	23
6.	Gage Records and Summary of Experimental Parameters from Figure 2 and Table 1, Shot 2407-7-2	27
7.	Gage Records and Summary of Experimental Parameters from Figure 2 and Table 1, Shot 2407-7-3	28
8.	Gage Records and Summary of Experimental Parameters from Figure 2 and Table 1, Shot 2407-7-4	29
9.	Stress Time Histories in PSDB at Depths of 2.15, 4.74, and 7.07 mm, Shot 2407-7-2	30
10.	Calculated Stress-Particle Velocity Trajectories for PSDB Mass Elements at Target Depths of 2.15, 4.74, and 7.07 mm, Shot 2407-7-2	31
11.	Calculated Stress-Specific Volume Trajectories for PSDB Mass Elements at Target Depths of 2.15, 4.74, and 7.07 mm, Shot 2407-7-2	32
12.	Stress-Time Histories in PSDB at Depths of 2.16, 4.76, and 7.09 mm, Shot 2407-7-3	33
13.	Calculated Stress-Particle Velocity Trajectories for PSDB Mass Elements at Target Depths of 2.16, 4.76, and 7.09 mm, Shot 2407-7-3	34

ILLUSTRATIONS (concluded)

14.	Calculated Stress-Specific Volume Trajectories for PSDB Mass Elements at Target Depths of 2.16, 4.76, and 7.09 mm, Shot 2407-7-3	35
15.	Stress-Time Histories in PSDB at Depths of 2.18, 4.82, and 7.09 mm, Shot 2407-7-4	36
16.	Calculated Stress-Particle Velocity Trajectory for a PSDB Mass Element at a Target Depth of 4.82 mm, Shot 2407-7-4	38
17.	Calculated Stress-Specific Volume Trajectory for a PSDB Mass Element at a Target Depth of 4.82 mm, Shot 2407-7-4	39
18.	PSDB Hugoniot and Dynamic Load-Release Trajectories from the Three Impact Experiments, Stress-Particle Velocity Representation	40
19.	PSDB Hugoniot and Dynamic Load-Release Trajectories from the Three Impact Experiments, Stress-Specific Volume Representation	41

TABLES

-	Conversion Factors for U.S. Customary to Metric (SL) Units of Measurement	4
1.	Target and Flier Thicknesses for Three PSDB Impact Experiments Shown Schematically in Figure 2	16

I INTRODUCTION

This study is one phase of a seven-part program having the overall objective of predicting the dynamic response of porous materials to rapid energy deposition. One prerequisite to a successful predictive capability is the construction of a set of constitutive relations describing the behavior of the porous material while porosity still exists and affects the material response. This dynamic "crush" curve and the associated release paths at low stress and energy levels can be obtained from mechanical impact experiments.

The objective of this work was to experimentally investigate the dynamic mechanical crush response, particularly during unloading, of PSDB^{*} loaded to less than full compaction. To do this, we performed three planar-impact gas gun experiments using PSDB targets containing multiple embedded ytterbium stress gages. Peak impact stresses were between 4 and 16 kbar.⁺ Two of the experiments, at peak stresses of 4 and 16 kbar, were nonattenuating wave shots in which thick PMMA[‡] fliers were used to prevent the unloading wave generated at the rear surface of the flier from catching the compression front in the instrumented portion of the targets. The third experiment, also at 16 kbar peak impact stress, was an attenuating wave shot in which the flier thickness was reduced to cause attenuation within the gaged area of the PSDB. The nonattenuating experiments were designed to provide good equation-of-state data, particularly during release; the purpose of the attenuation

^{*} Plasma-sprayed distended beryllium

⁺ 1 kbar = 10^{-1} GPa

[‡] Polymethyl methacrylate; in this case, Plexiglas Type II UVA

experiment was to provide profiles for checking the prediction capabilities of the PSDB constitutive models.

From each experiment, we obtained three stress-time profiles, each at a different depth in the target. Each set of profiles was reduced with the SRI Lagrange analysis code, GUINSY. From the GUINSY analyses we determined PSDB dynamic load-release trajectories in stress-particle velocity and stress-specific volume coordinates for each experiment.

The specimen material used in this program is described in Section II, below. Section III outlines the method of approach and describes the experimental and analytical techniques used in the experiments. Section IV summarizes the results, including two key findings: (1) the dynamic release paths for PSDB show significant irreversible compaction even at 4 kbar loading stress, and (2) in the nonattenuating experiments, several gage records showed an interesting stress overshoot, decay, and recompression after the initial compression, suggesting time-dependent pore collapse. These results are discussed in Section V. Section VI presents our conclusions and recommendations.

II SPECIMEN MATERIAL

The PSDB used in this program was a nonsintered, 15% nominal porosity plasma-sprayed material manufactured to match as nearly as possible the baseline material investigated by Lockheed Missile and Space Company (LMSC).¹ The LMSC specimens were manufactured from 10-44 μm powder supplied by Kawecki Berylco Industries, Inc.,^{*} as Lot No. KBI-0843. The powder was plasma-sprayed and machined for LMSC by Union Carbide Corporation,[†] according to Lockheed specifications designed to maintain specimen purity and uniformity.¹

The specimens used in the present study were manufactured from Kawecki Berylco beryllium powder, Lot No. KBI-2084, specified to match Lot No. KBI-0843. Figure 1 presents the quality control test report for this material. According to the manufacturer, this type of beryllium powder is produced by impact attrition or cold streaming, and as a result, is presumed to have a more equiaxed particle shape than high-purity electrolytic flake powder. The beryllium powder was plasma-sprayed into 15-inch-diameter disks (nominal), which were machined as required for our gas gun experiments[‡] at Union Carbide Corporation (UCC). The procedures followed by UCC in performing these operations are described below.[§]

The disks were sprayed on an aluminum substrate to about twice the

* Kawecki Berylco Industries, Inc., P.O. Box 429, Hazelton, Pa. 18201.

† Union Carbide Corporation, Linde Division, Indianapolis, Ind. 46224.

‡ The PSDB target shapes are described later in this section.

§ Based on UCC's test report to SRI.

Be Assay	99.17	
BeO	0.75	
C	0.057	
Fe	0.113	
Al	0.039	
Mg	0.045	
Si	0.020	
Mn	0.009	
Ti	0.017	
Cu	0.007	
Cr	0.008	
Ni	0.015	
All other metallic impurities	0.04	Max (each)
All other metallic impurities	0.25	Max (total)

Sieve Analysis:

+325 = T
-325 = 100.0%
-10 micron = 8.3%

Material in 98% minus 325 mesh—with approx. 8% minus 10 micron

MA-3163-9

FIGURE 1 QUALITY CONTROL TEST REPORT, BERYLLIUM POWDER KBI
LOT NO. 2084

3
desired thickness, and then removed from the substrate and sawed to shape. The density of a specimen of each disk was measured according to ASTM B-328. Each segment was then ground flat and parallel with a 60-grit aluminum oxide wheel using deionized water on a once-through basis as the coolant. The water was removed by placing the specimens in a vacuum furnace and heating to 300°C, until the vacuum was better than 10⁻⁵ torr. During the subsequent cooling, the furnace was backfilled with argon. The completed specimens were then sealed in plastic bags and shipped to SRI.

The resulting PSDB plates are 14.8 ± 0.5% porous, compared to a density of 1.85 gm/cc for solid (nonporous) beryllium. In the current experiments, the factor 0.5%, characterizing the reproducibility of the plasma-spraying operation, represents the maximum porosity variation within a target.

III METHOD OF APPROACH

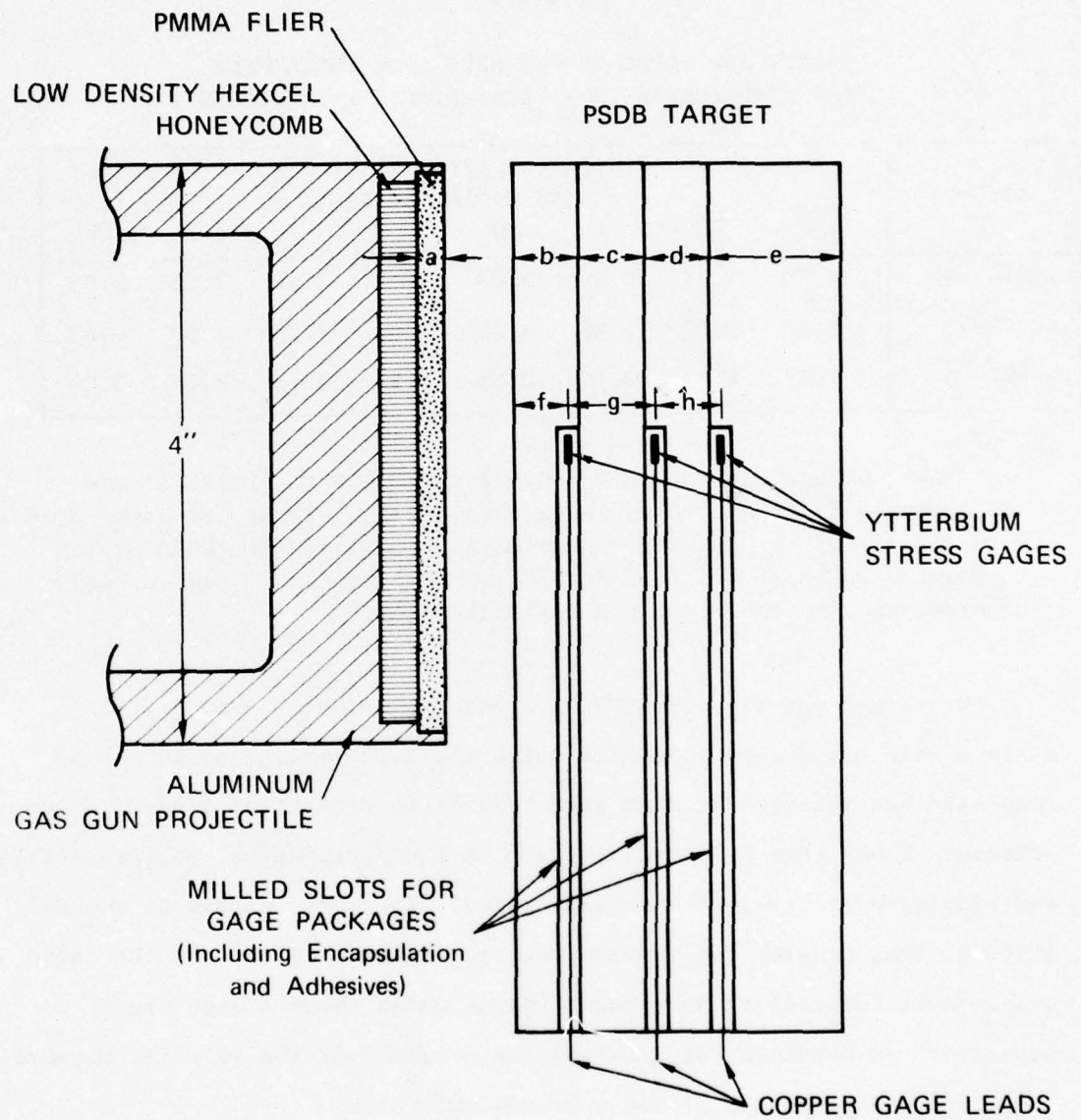
A. Experimental Techniques

The three PSDB experiments were performed on the SRI 4-inch gas gun. Figure 2 shows a side view of the basic experimental configuration used for all the shots, and Table 1 gives target and flier dimensions for the individual experiments. Figure 3 shows a front view of a completed target and an internal gage plane.

The flier plate for each experiment was a PMMA disk mounted in a standard SRI 7-inch-long, 2-kg (nominal) aluminum gas gun projectile. The fliers were supported across the back surface by Hexcel^{*} reinforced plastic honeycomb of 3/16-inch cell size and 0.004-inch wall thickness. The honeycomb supports the flier during the high acceleration phase of the projectile motion, but because of its very low areal density, permits the back surface of the flier to behave as a free surface. The rarefaction originating at this free surface generates the stress release in all three experiments.

Each target consisted of four stacked PSDB plates with an encapsulated ytterbium stress gage embedded at each interface, as shown in Figures 2 and 3. Each 15-inch-diameter plasma-sprayed blank was sawed radially into five equal parts, giving the plates a wedged shape, as shown in Figure 3. This unusual configuration minimizes the fabrication and material costs of the oversized targets (larger than the flier by about 5 cm at the gage lead exit points) required for satisfactory gage recording duration.

* Hexcel Products, Inc., 11711 Dublin Boulevard, Dublin, California



MA-3163-10

FIGURE 2 SCHEMATIC SIDE VIEW OF PROJECTILE AND TARGET CONFIGURATION USED IN ALL THREE PSDB IMPACT EXPERIMENTS

Table 1

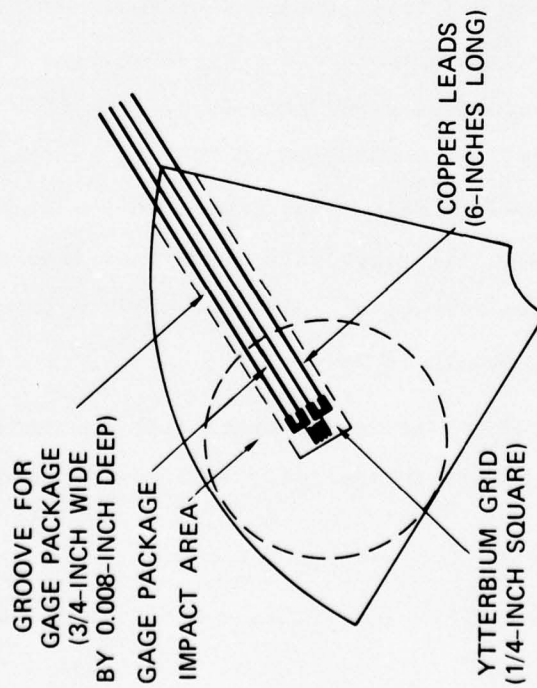
*
 TARGET AND FLIER THICKNESSES FOR THREE PSDB
 IMPACT EXPERIMENTS SHOWN SCHEMATICALLY IN FIGURE 2

Shot No.	Dimensions (from Figure 2) (in millimeters)							
	a	b	c	d	e	f	g	h
2407-7-2	4.50	2.27	2.30	2.28	4.65	2.15	2.59	2.33
2407-7-3	3.43	2.27	2.31	2.28	4.66	2.16	2.60	2.33
2407-7-4	1.27	2.34	2.30	2.28	4.66	2.18	2.64	2.27

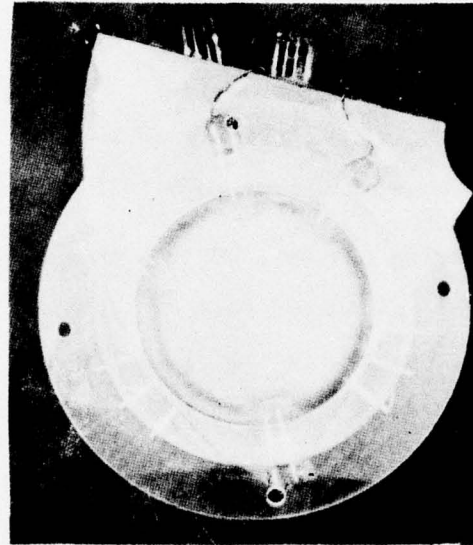
* The ytterbium gage elements are ≈ 0.051 mm (0.002 in.) thick. The gage packages (gage elements, leads, and encapsulation) are about 0.18 mm (0.007 in.) thick. The milled gage package slots in the PSDB plates are about 0.20 mm (0.008 in.) deep. An epoxy resin is used to bond the packages into the slots and fill all voids.

The target and flier thicknesses were selected to provide the maximum gage plane separation for which the load-release cycle can be completed and measured at each gage before the arrival of lateral edge effects. These edge effects originate at the periphery of the projectile and propagate in toward the target center. When they arrive at a gage station, they destroy the uniaxial nature of the flow and end the valid measurement interval at that gage. By using as large a gage plane separation as possible, we increase the accuracy of the velocity measurements and consequently, of the Lagrange analysis.

Target dimensions for the three experiments were standardized for cost-effectiveness. The nominal design thicknesses of the target components were 2.25 mm for the first three plates and 4.50 mm for the last (backer) plate. Table 1 gives actual thicknesses for each experiment.



TYPICAL GAGE PLANE (SCHEMATIC)



YTTERBIUM GAGE 1

YTTERBIUM GAGE 3

YTTERBIUM GAGE 2

MP-314525-6

FIGURE 3 GAGE PLANE SCHEMATIC AND PHOTOGRAPH OF COMPLETED TARGET

The backer plate is thicker to prevent the unloading wave generated at the free back surface of the target from arriving at the third gage before the flier-generated load-release cycle is completed. Although, as pointed out above, greater analysis accuracy would result with gage separations greater than 2.25 mm, the very high ratio of lateral rarefaction velocity to axial compression velocity in PSDB precluded this. Flier thicknesses, Table 1, were selected so that the shock would lead the release wave by about 1 μ sec at the third gage in the nonattenuating shots and would be overtaken near the first gage in the attenuating shot.

The gage elements were grids photoetched from nominal 0.002-inch (0.05 mm)-thick ytterbium foil. A 10-leg grid design fitting with a 6.4 mm square was used. The nominal electrical resistance of the grids was 1.35 ohms. The leads were four copper strips spot-welded to the outside elements of each grid. Figure 3 shows the grid-lead configuration.

In the high-stress, nonattenuating shot (Shot 2407-7-2), a different gage encapsulation material was tried for each of the three gages, because previous work² indicated that gage survivability might be a problem. The materials used were 0.003-inch (0.075 mm) fiberglass, 0.001-inch (0.025 mm) mica, and 0.001-inch (0.025 mm) Kapton^{*} polyimide film. All functioned satisfactorily. Therefore, in the next two experiments, we encapsulated all gages with 0.003-inch fiberglass, the most convenient material to work with. All gage package thicknesses were approximately 0.007 inch (0.18 mm).

The gages were located one above the other with the center of each grid element on the axis normal to the impact plane and passing through

* E. I. Du Pont de Nemours and Co. (Inc.), Film Department, Wilmington, Delaware 19898.

the middle of the intended impact circle. To reduce the tendency for electrical cross talk between gages, we rotated the packages about 20 degrees from one another. The gage packages were epoxied into slots milled in the PSDB plates* to minimize the extent and thickness of internal bond lines and plate separation in the targets. Homalite[†] 1100 was used for all gage and plate bonding. A bolt, reestablishing contact between the plates, was used to reduce electrical noise during the shot.

No efforts were made to remove any densified PSDB surface layers caused by specimen machining. If densification did occur, it was not obvious from microscopic examination of our specimens, although some variations, not identifiable as densification, were noted to a depth of a few mils. We assumed that these surface variations, if significant, simply provided additional gage encapsulation. As long as the effect is equal at each gage, the accuracy of the calculated load or release trajectories will not be reduced, since both are determined by relative velocities between gages.

The copper gage leads were brought out through the sides of the target in the gage plane. In most impact experiments, including the current ones, this lead configuration allows the stress gages to survive and record until the shock signal reaches the lead exit point at the edge of the target. To ensure that this occurs after completion of the intended measurement interval, we used the oversized, wedge-shaped PSDB targets described earlier.

* See Figure 2 for identification of the plates containing slots.

[†] Homalite Corporation, 1113 Brookside Drive, Wilmington, Delaware 19804

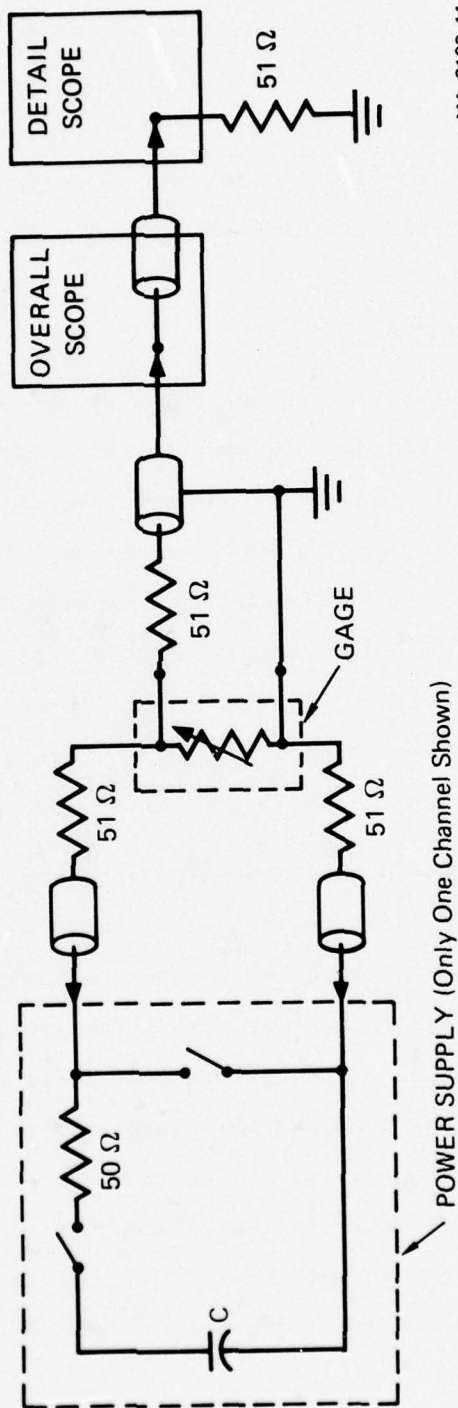
The target photograph in Figure 3 shows many of the features described above, including the fiberglass-encapsulated gage leads extending from the side of the target, the rotated (offset) exit points for the three gages, and the grounding bolt. Also visible are instrumentation trigger pins and switches on an near the impact surface (the flush pin pairs were not used).

A three-channel, constant current power supply, Pulsar Model 301,^{*} was used to energize the stress gages.[†] A detail and backup oscilloscope monitored each gage. All scopes and power supplies were triggered from radial pins located ahead of the target impact plane and extending about 1/16 inch (1.6 mm) into the projectile flight path (see Figure 3). Figure 4 shows a schematic diagram of the instrumentation circuit for one gage. References 3-5 give additional details of stress gages and recording techniques.

Because of the toxicity of the finely divided beryllium expected from postshot fragmentation of the target, we followed special gun firing procedures recommended by the SRI Health and Safety Department to prevent exposure of personnel to beryllium dust. These procedures included: strengthening the gasket seal between the target chamber and the projectile catcher tank to prevent venting into the gun room; installing submicron disposable filters ahead of the vacuum pump in the target chamber-catcher tank vent line; supplying all persons present during firing with respirators having submicron filters; supplying all persons involved in opening and decontaminating the gun facility with protective

^{*} Pulsar Instrument Company, 650 Vaqueros, Sunnyvale, California 94086.

[†] In Shot 2407-7-2, the first gage was run in a two-lead bridge mode because of a lead failure after shot construction. See reference 3 for a description of this technique.



MA-3163-11

FIGURE 4 GAGE CIRCUIT, SCHEMATIC REPRESENTATION

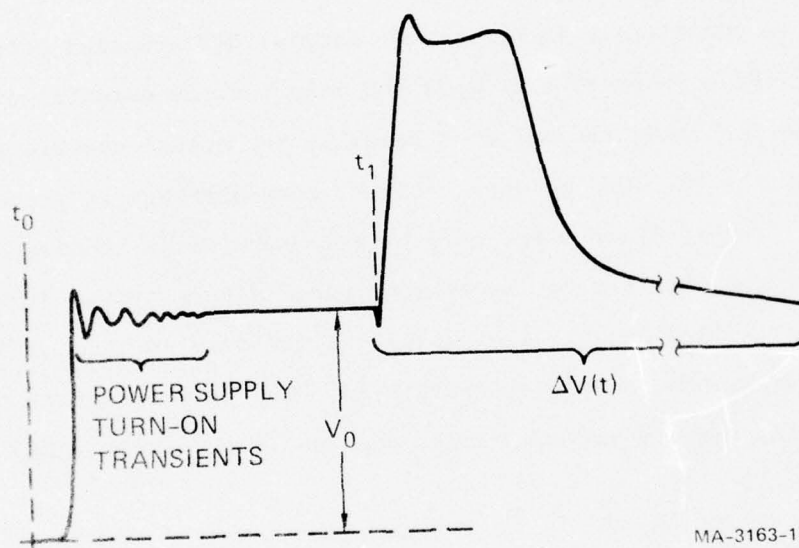
disposable clothing; following cleanup procedures designed to keep beryllium dust from becoming airborne; using approved beryllium disposal methods for all shot debris; and taking air samples throughout the firing and cleanup procedures until the facility was declared decontaminated. A test shot without a beryllium target was performed to verify the effectiveness of the sealing and venting steps.

B. Analytical Techniques

Figure 5 is a schematic representation of the basic features of the ytterbium stress gage records obtained in this program. The first voltage step, after power supply turn-on transients have died out, is the potential developed across the gage element in response to the power supply constant current and the initial gage resistance. The subsequent deflection is the change in potential resulting from stress-induced resistance changes in the gage element. Figure 5 is the stress gage record that would be seen on the overall oscilloscope; the detail oscilloscope shows the stress-induced portion of the signal at higher magnification.

The stress gage records are converted to stress-time histories by the following procedure. The portion of the record containing the stress information, $\Delta V(t)$, is digitized and key-punched on a Telereadex^{*} film reader and associated recording equipment. The arbitrary film reader units are converted to volts and microseconds using direct current voltage calibration steps recorded immediately after the shot and calibrated time marks recorded during the shot as trace blanks. The signal in volts is then related to resistance changes at the gage element by a direct current Kirchhoff loop analysis. The analysis accounts for the deviations from constant current and for the variable shunting of the

* Telereadex Type 29E, Data Instruments, A Division of Telecomputing Corporation, 12838 Saticoy Street, North Hollywood, California.



MA-3163-12

FIGURE 5 SCHEMATIC REPRESENTATION OF A PIEZORESISTANT STRESS GAGE RECORD

gage element by the scopes, both caused by the stress-induced changes in circuit resistances during the shot. The resistance-time profiles obtained by the preceding operations are then converted to stress-time profiles by use of dynamic ytterbium stress calibration data measured by Ginsberg.⁵

We calculated the stress-particle velocity and stress-specific volume trajectories from the three stress-time histories obtained in each experiment with the SRI Lagrange analysis code GUINSY.⁶ This code uses stress or particle velocity histories obtained at various depths in a flow to numerically integrate the partial differential equations expressing the conservation of mass and momentum for uniaxial displacements. The resulting trajectories describe the actual dynamic states attained during the load-release cycle by mass elements at or between the gages. The analysis makes no a priori assumptions concerning the response of the specimen or the thermodynamic nature of the flow. Accuracy is limited only by the quality of the data and the number of histories available to define derivatives. The latter factor is especially important for rapidly varying flows, such as in the attenuating wave experiment.

The Lagrange gage technique offers several advantages over conventional shock measurement techniques. For example, the point at the top of a GUINSY loading trajectory is a better defined measurement of the dynamic compression state, often called the Hugoniot state,^{*} than can

* Experimentally defined, the Hugoniot states are states achievable from a given initial state by rapid (impact) compressions. For some rate-dependent materials, such states are not equilibrium states and, hence, characterize the response only to the specific applied loading conditions. Such states are not true thermodynamic Hugoniot points (although they are sometimes referred to as such), but are valid specifications of material response at the applied loading rates.

be obtained from conventional shock wave techniques that rely on front and rear surface measurements. This is because the GUINSY analysis is valid for any flow, whereas the analyses used with surface measurements require some specific flow assumption, such as steady-state wave propagation, that often does not hold in real materials. Another advantage of the Lagrange analysis technique is that the dynamic unloading trajectory obtained from a single Lagrange shot would require a series of experiments when using conventional techniques. Furthermore, the validity considerations discussed for Hugoniot measurements also apply to release-state measurements. A fourth advantage of the Lagrange analysis techniques is that if the specimen response is time-dependent, interpretation of the GUINSY results will often indicate the magnitude of the time constant.

IV RESULTS

Figures 6, 7, and 8 show the actual records obtained for each gage and summarize the experimental parameters for each experiment. In both nonattenuating shots, an unexpected structure appears between the primary compression and the release phases: a fairly rapid overshoot and release followed by a slower recompression. This structure is interpreted in Section V. The source of the high-frequency noise in the attenuating wave shot, Figure 8, is uncertain but may be an imperfect electrical ground.

Figure 9 shows the three gage records for Shot 2407-7-2, the high-stress, nonattenuating wave experiment, converted to stress-time coordinates and plotted on a common time scale. The zero time in this plot is arbitrary; it is not impact time. Figures 10 and 11 give the stress-particle velocity and stress-specific volume trajectories at each gage position, calculated by the GUINSY analysis. The analysis included the wave structure at the top of the compression pulse.

Figure 12 shows three stress profiles for Shot 2407-7-3, the low-stress, nonattenuating experiment, with the structure at the top omitted. The zero time is again arbitrary. Figures 13 and 14 give the stress-particle velocity and stress-specific volume trajectories at each gage location calculated by the GUINSY analysis. The only effect on the calculated trajectories of omitting the structure is a possible small displacement of the starting point for the release curve (discussed in Section V).

Figure 15 shows the stress histories for Shot 2407-7-4, the attenuating wave experiment. The high-frequency noise apparent in the

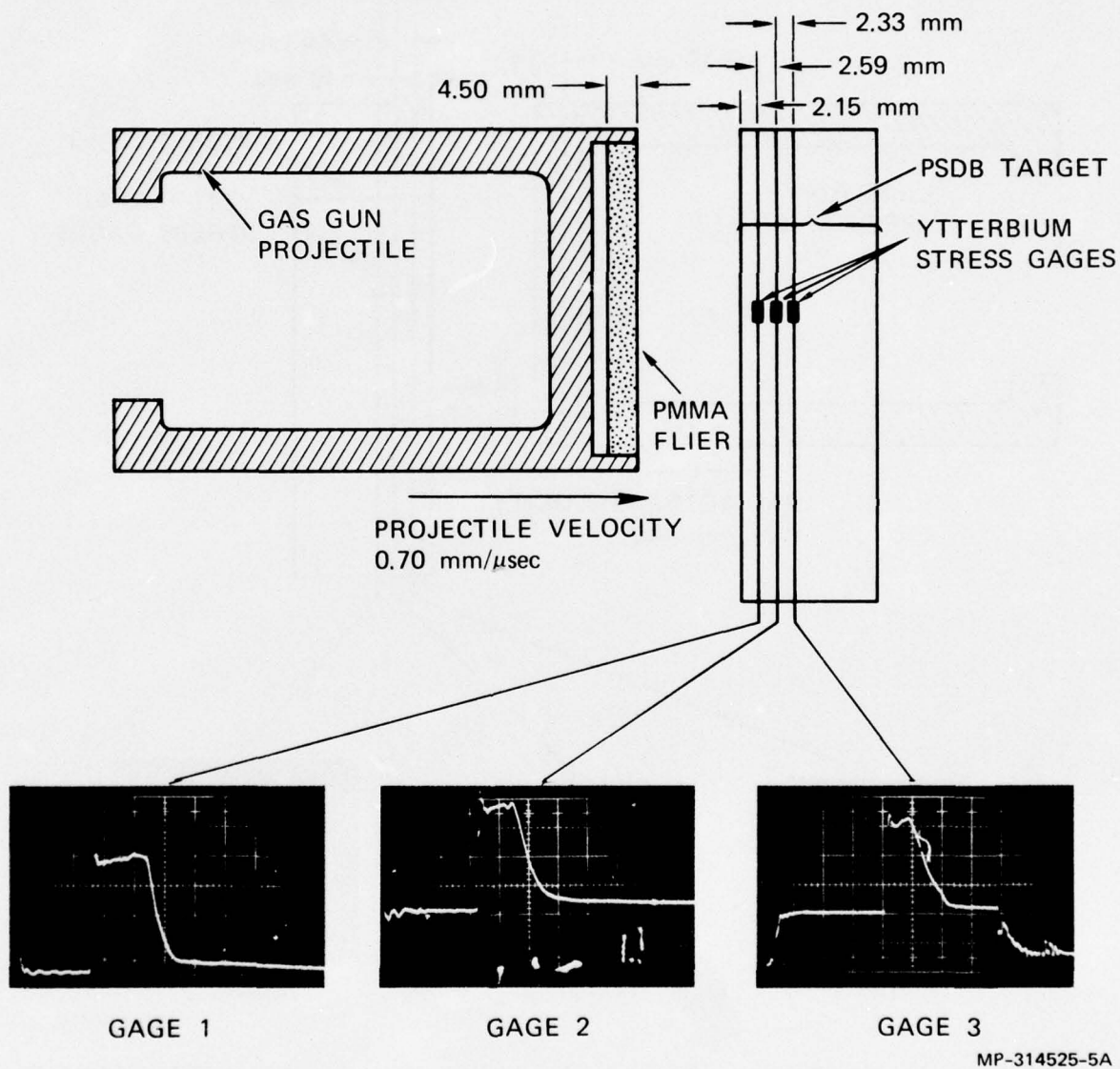
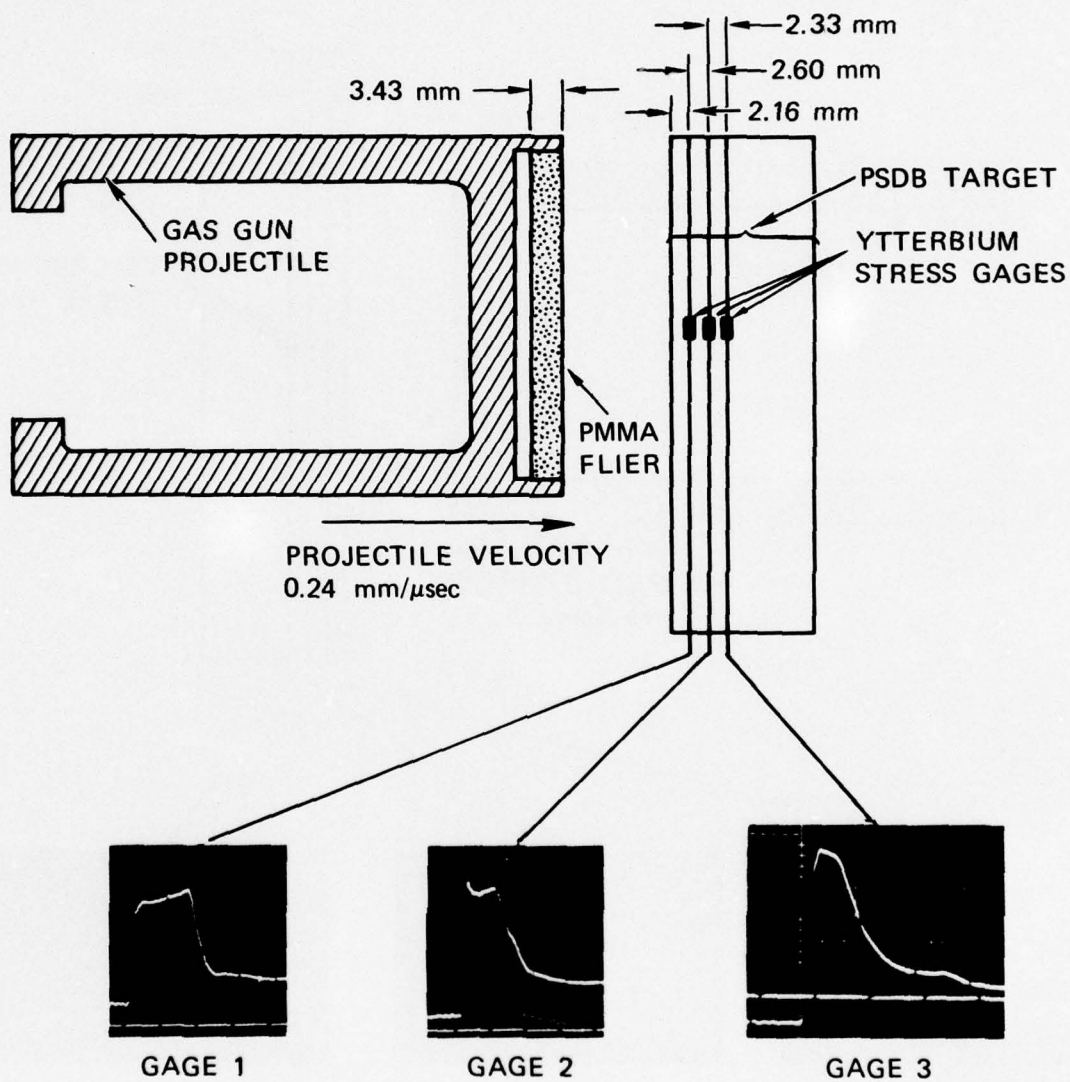
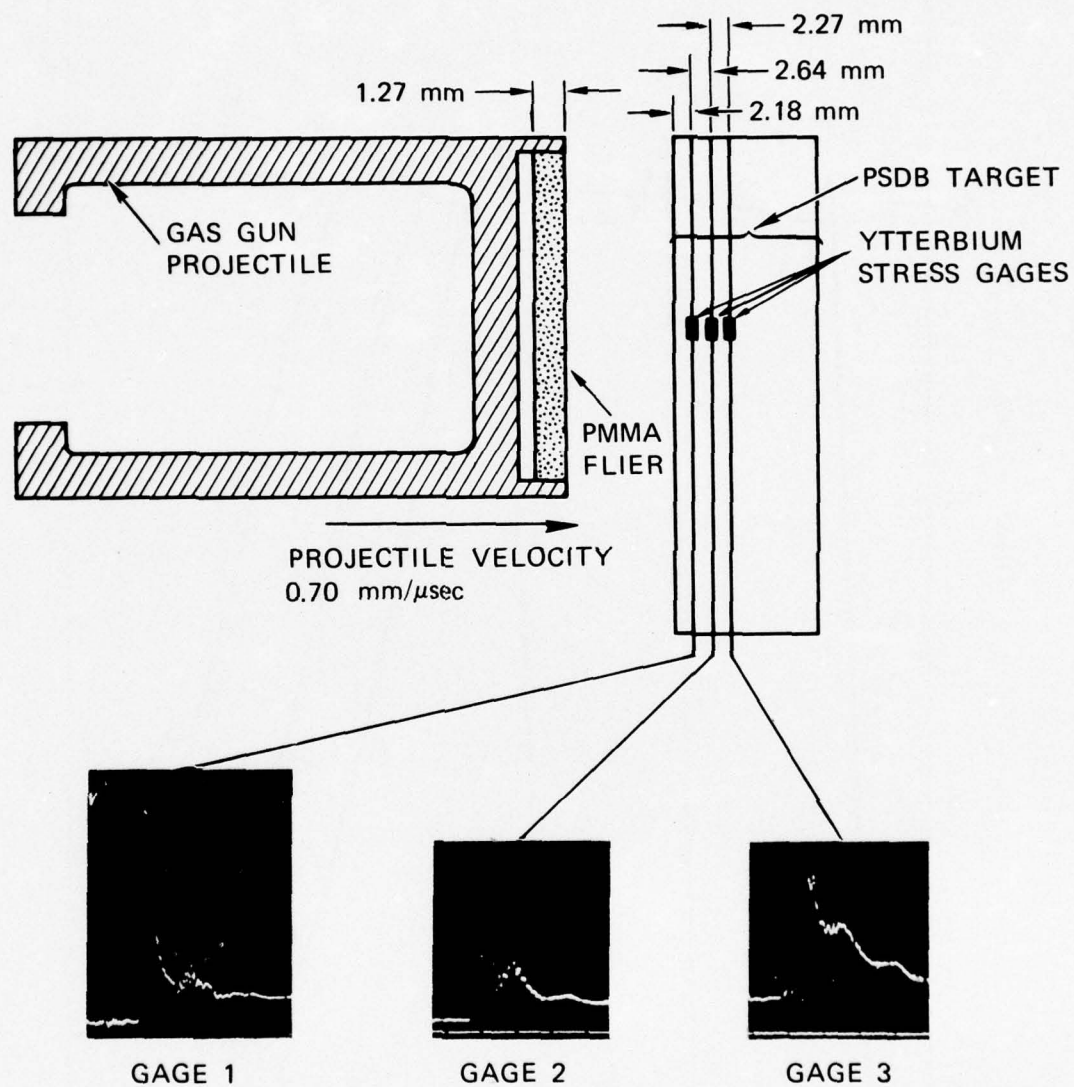


FIGURE 6 GAGE RECORDS AND SUMMARY OF EXPERIMENTAL PARAMETERS FROM FIGURE 2 AND TABLE 1, SHOT 2407-7-2



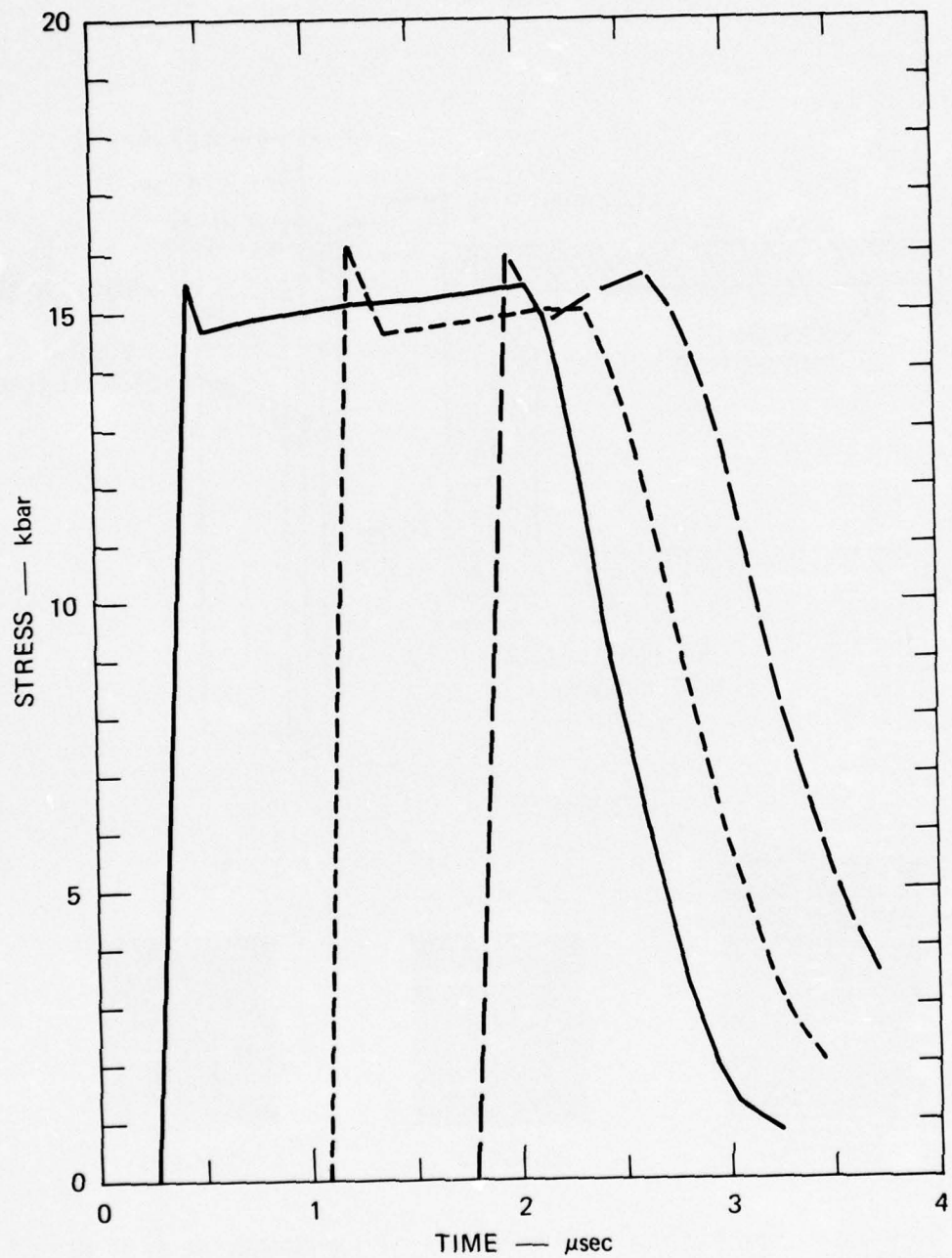
MP-3163-14

FIGURE 7 GAGE RECORDS AND SUMMARY OF EXPERIMENTAL PARAMETERS FROM FIGURE 2 AND TABLE 1, SHOT 2407-7-3



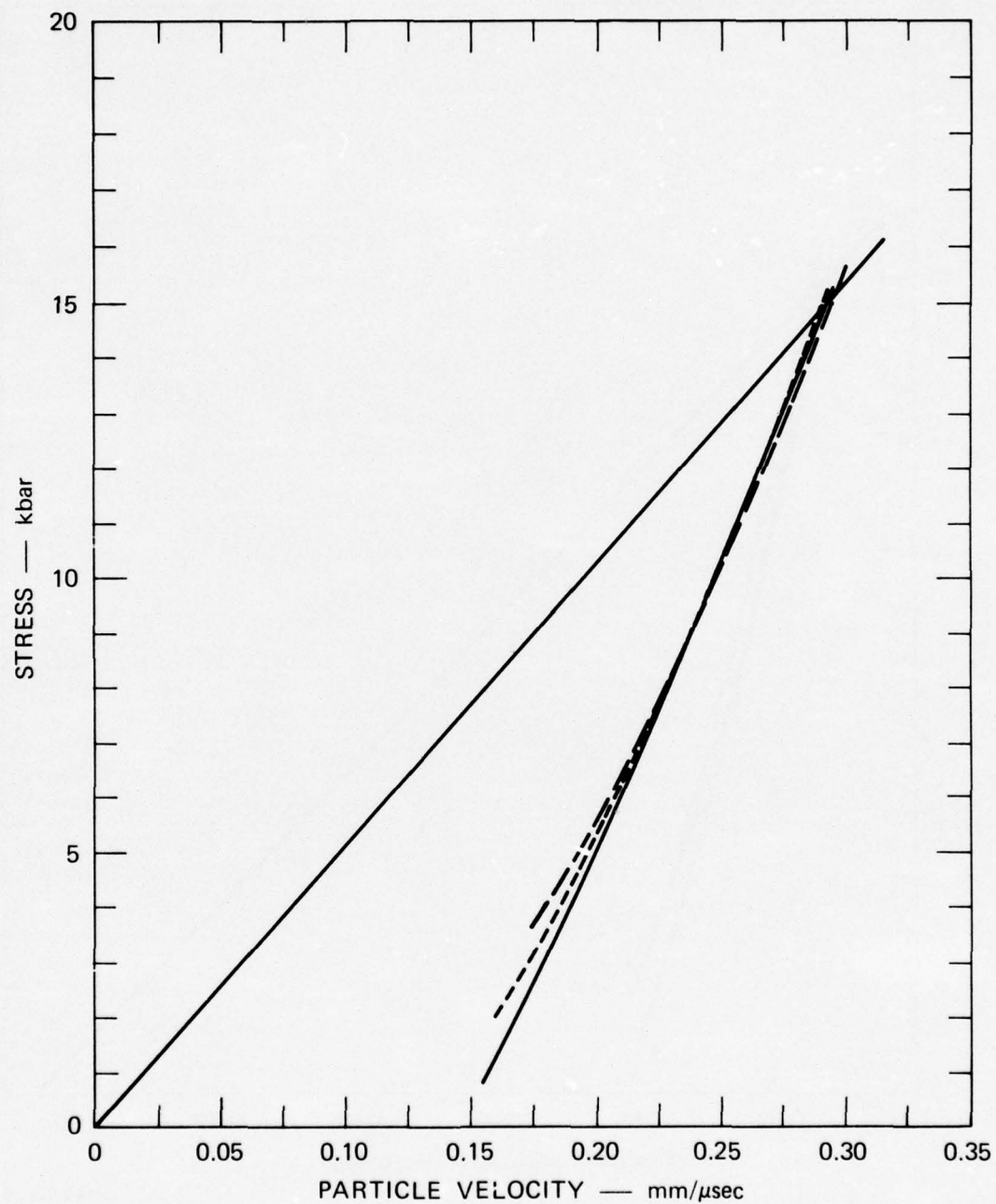
MP-3163-15

FIGURE 8 GAGE RECORDS AND SUMMARY OF EXPERIMENTAL PARAMETERS FROM FIGURE 2 AND TABLE 1, SHOT 2407-7-4



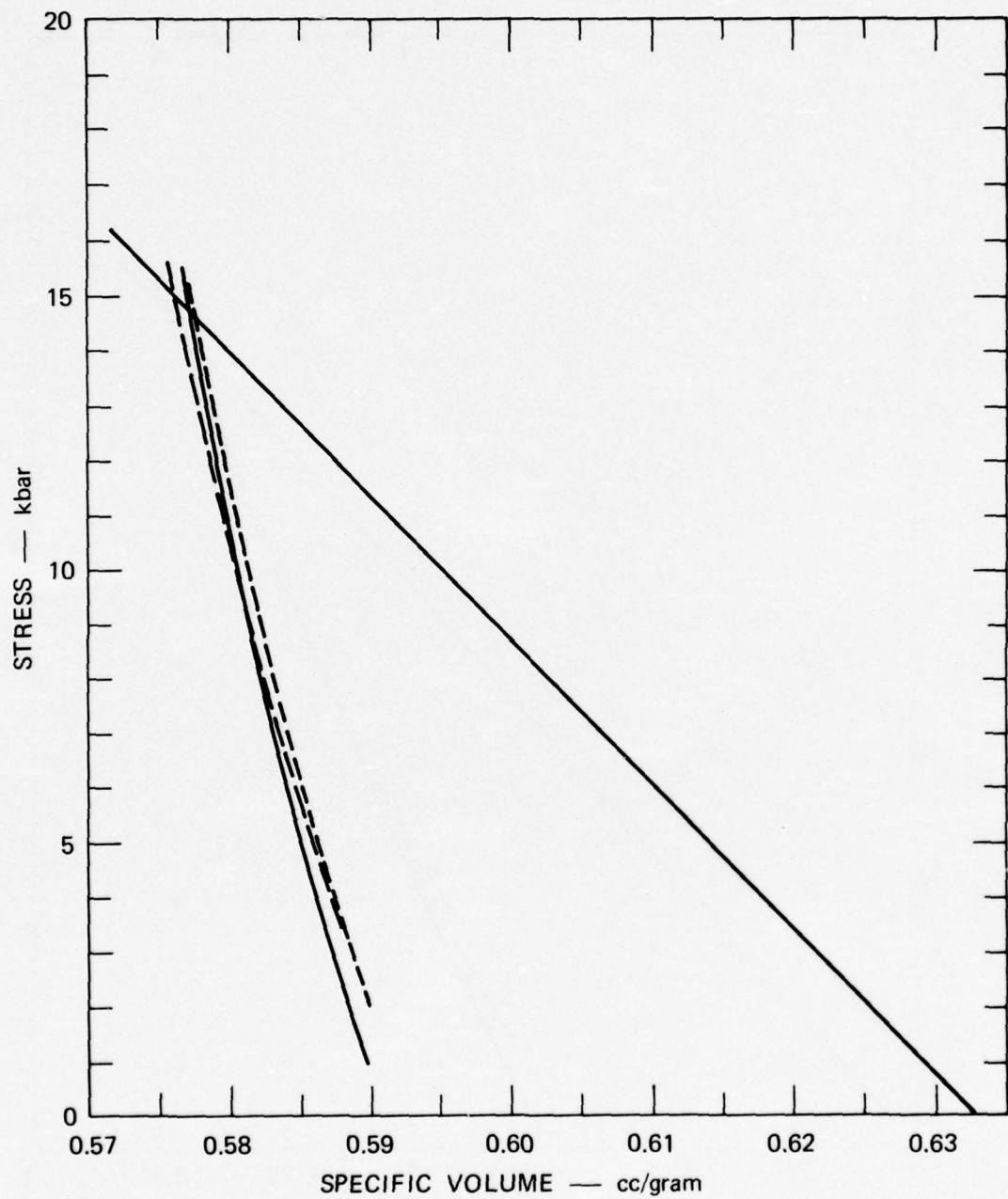
MA-3163-16

FIGURE 9 STRESS TIME HISTORIES IN PSDB AT DEPTHS OF 2.15, 4.74, AND 7.07 mm, SHOT 2407-7-2



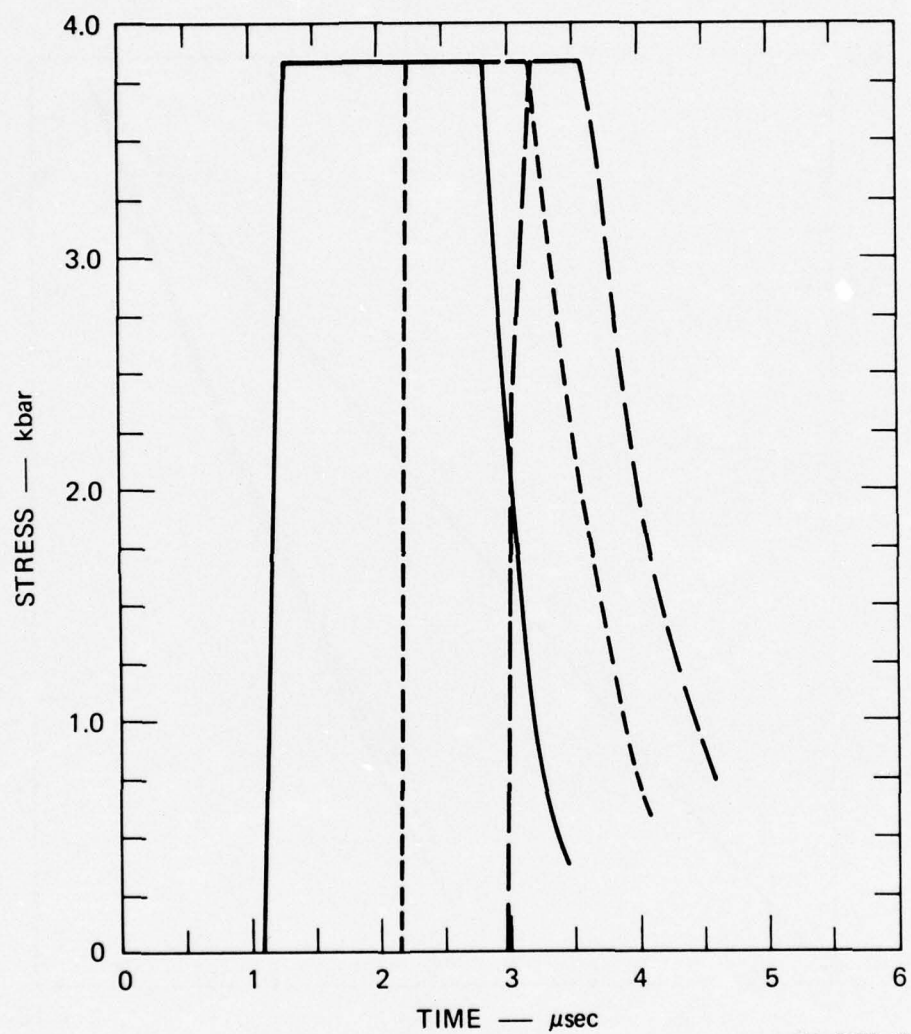
MA-3163-17

FIGURE 10 CALCULATED STRESS-PARTICLE VELOCITY TRAJECTORIES FOR PSDB MASS ELEMENTS AT TARGET DEPTHS OF 2.15, 4.74, AND 7.07 mm, SHOT 2407-7-2



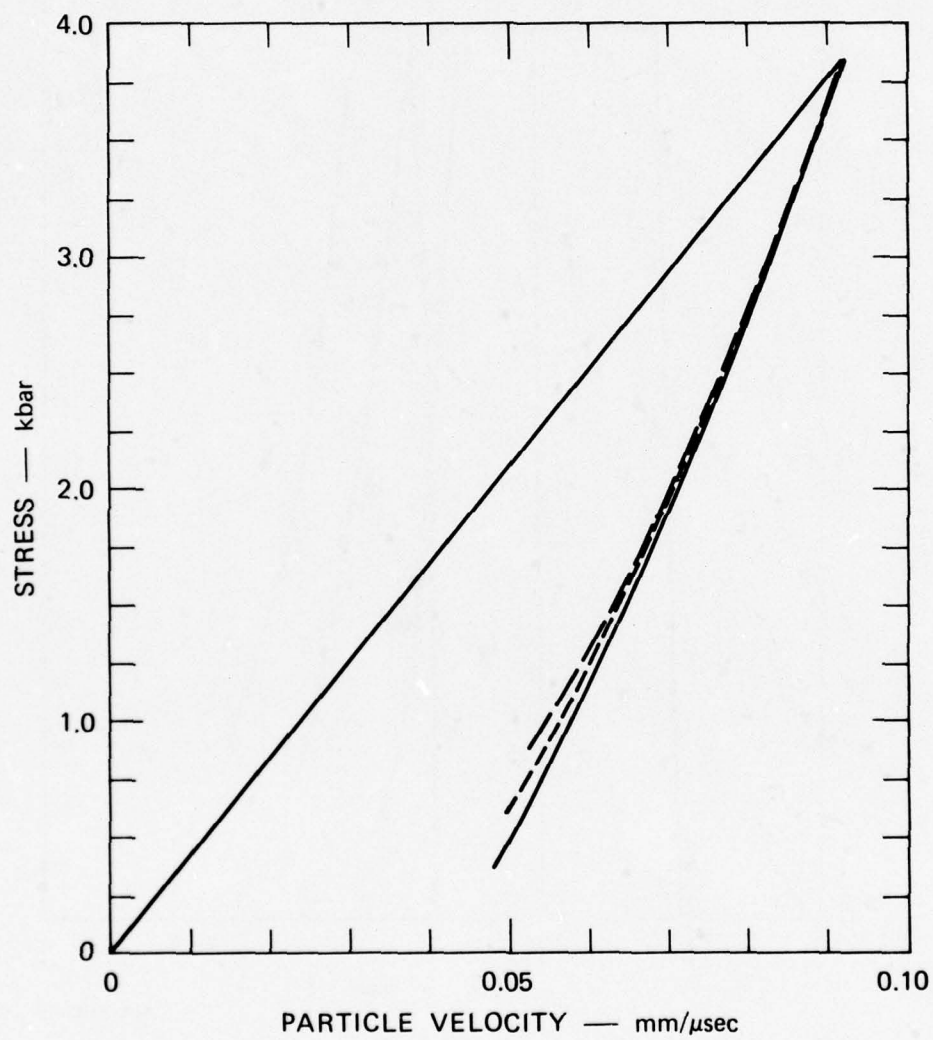
MA-3163-18

FIGURE 11 CALCULATED STRESS-SPECIFIC VOLUME TRAJECTORIES FOR PSDB MASS ELEMENTS AT TARGET DEPTHS OF 2.15, 4.74, AND 7.07 mm, SHOT 2407-7-2



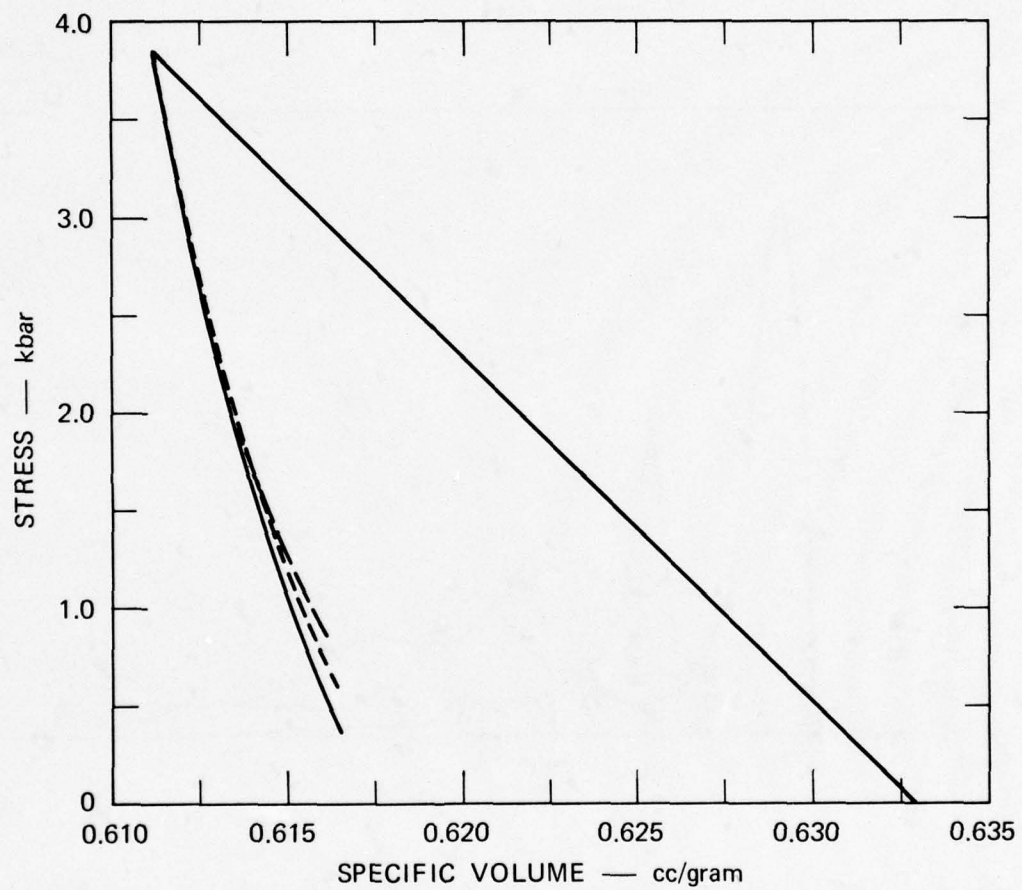
MA-3163-19

FIGURE 12 STRESS-TIME HISTORIES IN PSDB AT DEPTHS OF 2.16, 4.76, AND 7.09 mm, SHOT 2407-7-3



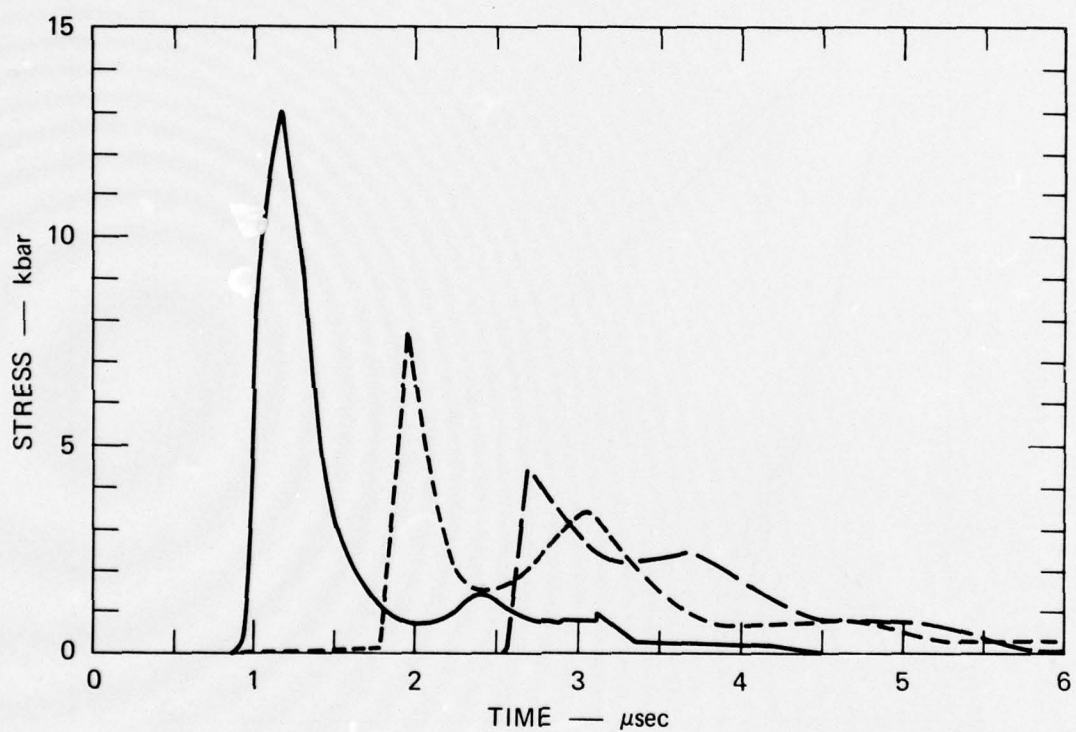
MA-3163-20

FIGURE 13 CALCULATED STRESS-PARTICLE VELOCITY TRAJECTORIES FOR PSDB MASS ELEMENTS AT TARGET DEPTHS OF 2.16, 4.76, AND 7.09 mm, SHOT 2407-7-3



MA-3163-21

FIGURE 14 CALCULATED STRESS-SPECIFIC VOLUME TRAJECTORIES FOR PSDB MASS ELEMENTS AT TARGET DEPTHS OF 2.16, 4.76, AND 7.09 mm, SHOT 2407-7-3

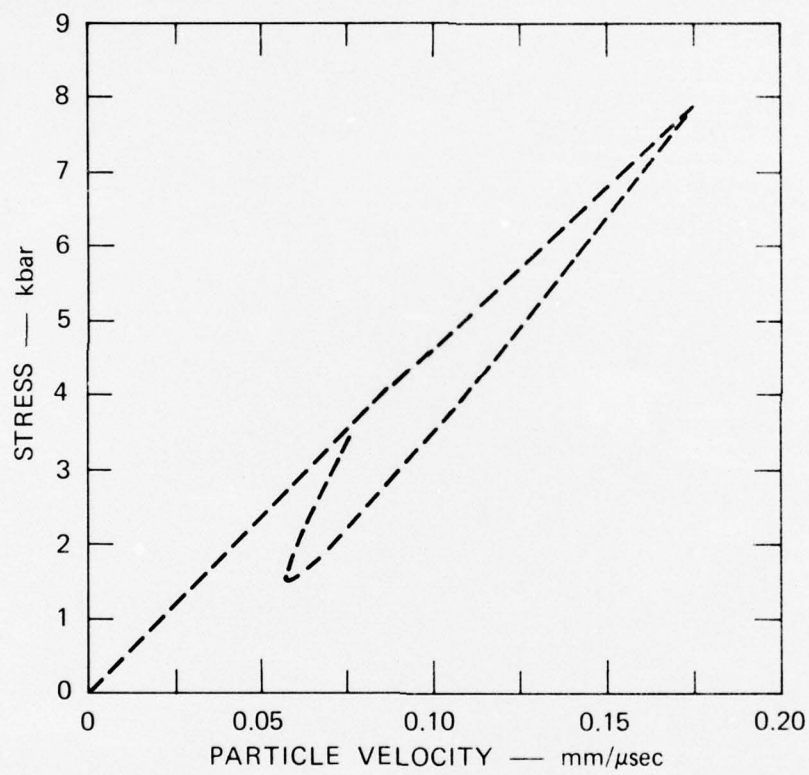


MA-3163-22

FIGURE 15 STRESS-TIME HISTORIES IN PSDB AT DEPTHS OF 2.18, 4.82, AND 7.09 mm, SHOT 2407-7-4

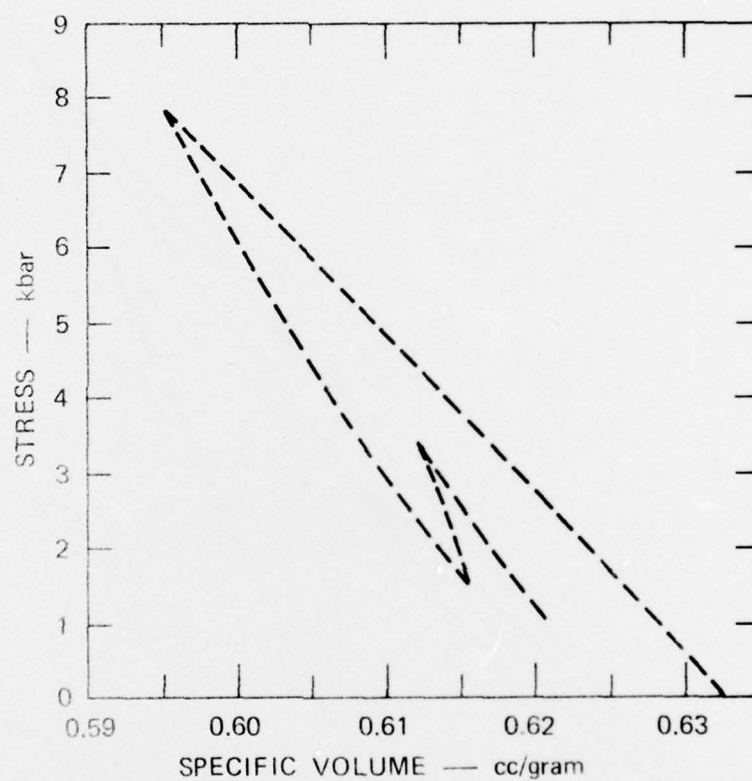
oscilloscope records was deleted during the Telereadex digitizing operation. The origin of the time scale is again arbitrary. The stress histories were used in conjunction with the GUINSY analysis to generate a stress-particle velocity and a stress-specific volume trajectory at the middle gage position as shown in Figures 16 and 17.

For convenience, the stress-particle velocity and stress-specific volume trajectories for all three experiments are plotted together, in Figures 18 and 19.



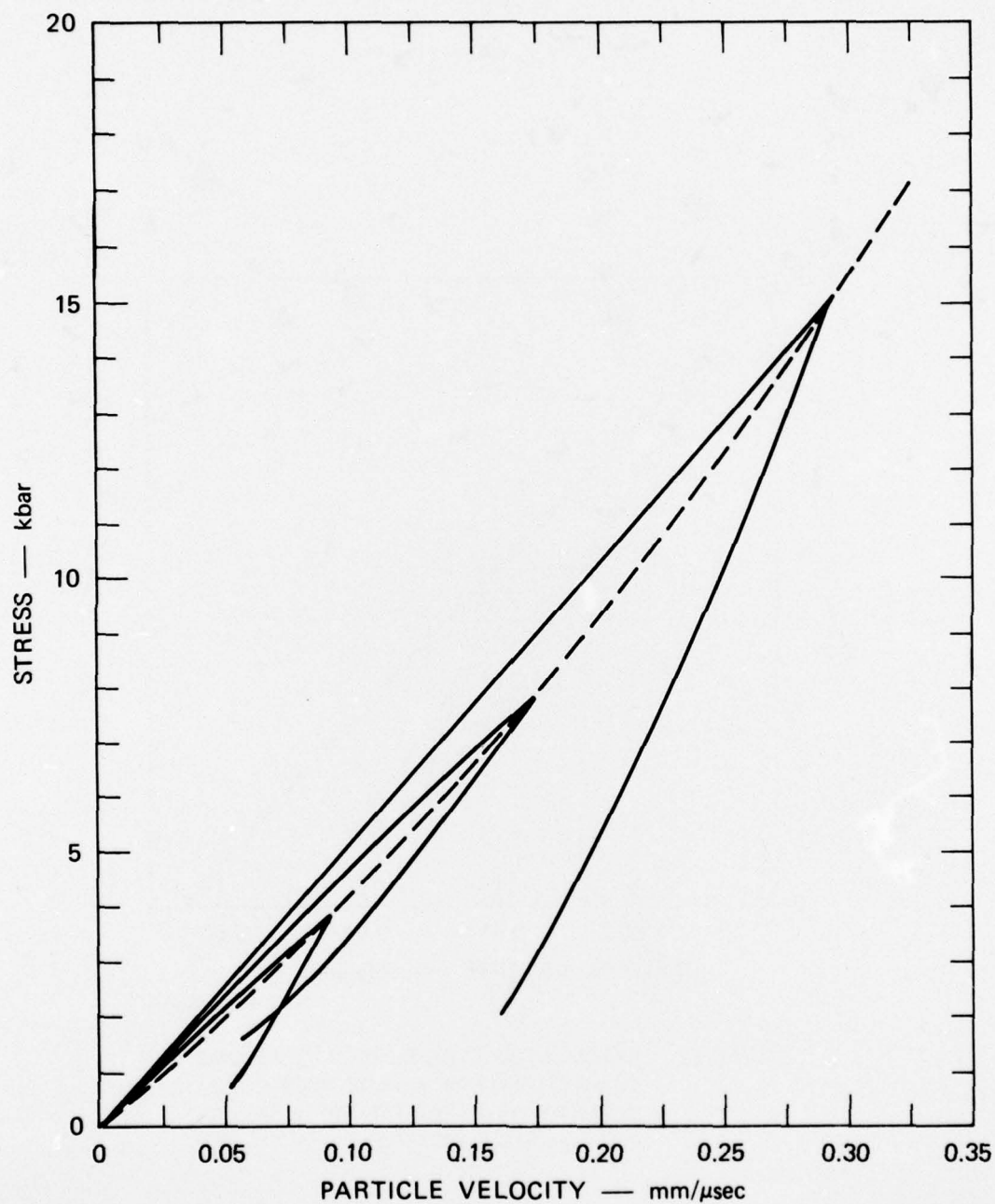
MA-3163-23

FIGURE 16 CALCULATED STRESS-PARTICLE VELOCITY TRAJECTORY FOR A PSDB MASS ELEMENT AT A TARGET DEPTH OF 4.82 mm, SHOT 2407-7-4



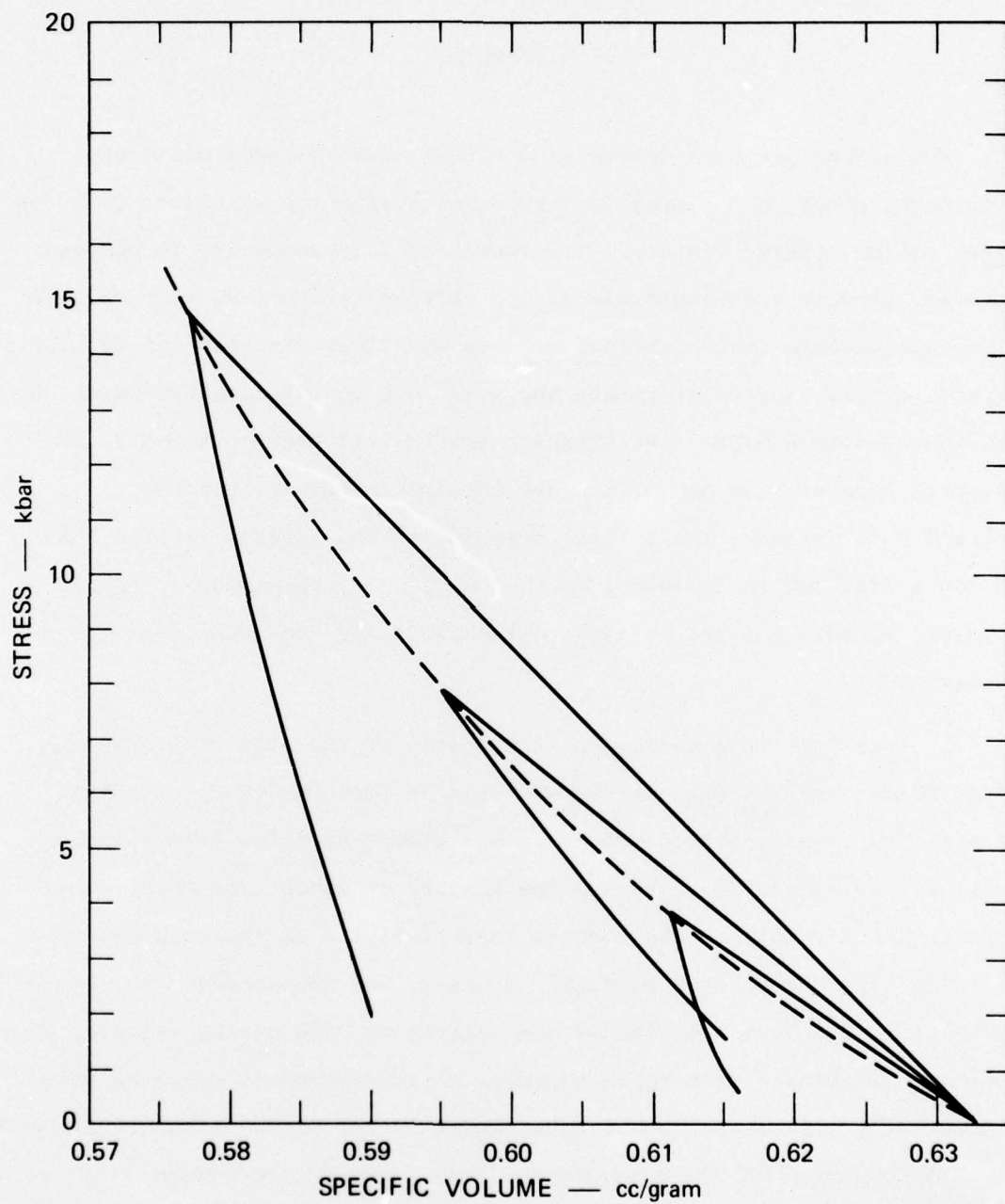
MA-3163-24

FIGURE 17 CALCULATED STRESS-SPECIFIC VOLUME
TRAJECTORY FOR A PSDB MASS
ELEMENT AT A TARGET DEPTH OF
4.82 mm, SHOT 2407-7-4



MA-3163-25

FIGURE 18 PSDB HUGONIOT AND DYNAMIC LOAD-RELEASE TRAJECTORIES FROM THE THREE IMPACT EXPERIMENTS, STRESS-PARTICLE VELOCITY REPRESENTATION



MA-3163-26

FIGURE 19 PSDB HUGONIOT AND DYNAMIC LOAD-RELEASE TRAJECTORIES FROM THE THREE IMPACT EXPERIMENTS, STRESS-SPECIFIC VOLUME REPRESENTATION

V DISCUSSION

The stress profiles in the nonattenuating wave experiments show overshoot, decay, and slower recompression during the so-called flat-top phase of the loading history. The source of this structure is unknown. However, because the time-scale of the effects is too long to correlate with gage package reverberations or with any other experimental artifacts we have considered, we attribute the structure to physical processes in the impact-loaded PSDB. For example, the initial overshoot and decay strongly suggest time-dependent pore collapse; that is, because of delayed pore failure, the initial response to the rapidly applied load is too stiff, but is followed, as the pores fail, by stress relaxation. However, we have not yet satisfactorily explained the subsequent recompression.

By treating the structure as a property of the flow and including it in GUINSY, as was done in the analysis of Shot 2407-7-2, we obtain interesting stress-particle velocity and stress-specific volume features (see Figures 10 and 11). During the initial overshoot and decay, the PSDB apparently retains the modulus characteristic of the original compression, the uncompacted modulus. However, for the subsequent recompression it displays the modulus characterizing PSDB during release, the compacted modulus. This again suggests a time-dependent crushing with a compaction time equal to the spike width, a few tenths of a microsecond.

The accuracy of the experimental data, however, and especially, of the GUINSY analysis, is much reduced for the small, slow-stress variations discussed here. Consequently, we must conclude that although the modulus variations noted are very interesting, they may not be significant compared with the overall experimental error, which includes both the measurement and the unknown analysis contributions.

For these reasons and because the source of the effect is unknown, and possibly an artifact of the experimental technique, the overshoot-decay-recompression structure was omitted in the analysis of Shot 2407-7-3. This omission has a negligible effect on the calculated loading and release trajectories, since these are determined primarily by the propagation characteristics of the compression and release fronts. The only uncertainty introduced is the stress level at which to terminate the loading. This uncertainty can introduce an error in the Hugoniot state and in the origin of the release curve equal to, at most, half the amplitude of the oscillation. If the modulus during this period is that of compacted PSDB, there is no displacement at all of the release curve.

Stress profiles for the attenuating wave experiment, Shot 2407-7-4, contain a secondary peak during unloading. This peak is believed to be unrelated to the structure in the nonattenuating experiments and is assumed to result from the interaction of the overtaking rarefaction with the compression front. By using a simple two-modulus constitutive relation in conjunction with PUFF, a one-dimensional artificial viscosity wave propagation code, we have shown that this behavior is characteristic of a material that stiffens significantly in the shock front.⁷ A crushable, highly porous substance like PSDB has this property. The Lagrange analysis remains valid under these conditions, although accuracy in analyzing the substructure is reduced.

Because of the rapid stress decay in the attenuating experiment, Shot 2407-7-4, the flow characterization provided by the three gage records is not as complete as for the nonattenuating experiments. Therefore, the GUINSY stress-particle velocity and stress-specific volume trajectories derived are not as reliable as those for the two nonattenuating experiments, but for completeness, we have included the results from this shot. However, since the purpose of this shot was to generate

profiles for checking the prediction capabilities of PSDB models, we have not reported trajectories at each gage location, but have presented only the results at the middle of the instrumented interval (at Gage 2).

VI CONCLUSIONS AND RECOMMENDATIONS

7

The two nonattenuating wave experiments have provided dynamic compression and release trajectories in the stress-particle velocity and stress-specific volume planes for partially compacted PSDB. These trajectories show that PSDB exhibits irreversible compaction at stresses as low as 4 kbar. The use of the trajectories to model the crush behavior of PSDB at low stresses and energy levels is covered in Volume 3 of this report series (see Preface).

Several of the gage records from the nonattenuating experiments show stress overshoot, decay, and slow recompression following the initial compression. Although the limited amount of data obtained in this study is not sufficient to prove that this structure is experimentally significant, it is not easily explained as an experimental artifact and may well reflect a complex process in the PSDB, such as time-dependent pore collapse. Additional experiments would be necessary to investigate this hypothesis. We recommend performing such experiments if an explanation of the actual mechanism of pore collapse in PSDB is required.

The nonattenuating wave experiment provided stress profiles for checking PSDB constitutive models. In addition, this experiment provided another compression and release trajectory. These trajectories show less hysteresis and, hence, less irreversible compaction than those obtained in the nonattenuating experiments. Additional work is required to determine whether the reduced hysteresis is a result of time dependence of the compaction reversibility in PSDB or simply reflects the diminished accuracy of the Lagrangian analysis when applied to an attenuating wave experiment.

Volume 1 of this report series discusses the significance of the present work in the general characterization of the dynamic response of porous materials.

VII REFERENCES

1. A. O. Burford, Lockheed Missile and Space Company, Sunnyvale, California, private communication.
2. W. N. Isbell, Lawrence Livermore Laboratory, Livermore, California, private communication.
3. W. J. Murri, D. R. Curran, C. F. Petersen, and R. C. Crewdson, "Response of Solids to Shock Waves," in *Advances in High-Pressure Research*, Vol. 4, ed. R. H. Wentorf, Jr., Academic Press, 1974.
4. J. T. Rosenberg, "Development of a Piezoresistant Transducer to Measure Stress-Time Output of Small Detonators," AD 912487-L, Final Report, Stanford Research Institute, for Picatinny Arsenal, Dover, New Jersey, March 1973.
5. M. J. Ginsberg, "Effects of Stress on the Electrical Resistance of Ytterbium and Calibration of Ytterbium Stress Transducers," Draft Final Report, Stanford Research Institute, Contract No. DNA 001-72-C-0146, August 1973.
6. L. Seaman, "Lagrangian Analysis for Multiple Stress or Particle Velocity Gages in Attenuating Waves," *J. of App. Physics*, Vol. 45, No. 10, October 1973, pp. 4303-4314.
7. J. T. Rosenberg, private communication.

DISTRIBUTION LIST

DEPARTMENT OF DEFENSE

Director
Defense Advanced Research Project Agency
ATTN: Strategic Tech. Office

Defense Communication Engineer Center
ATTN: Code 720, John Worthington

Director
Defense Communications Agency
ATTN: NMCSSC Code 510

Defense Documentation Center
12cy ATTN: TC

Director
Defense Intelligence Agency
ATTN: DI-7D
ATTN: DT-1C, Nuc. Eng. Branch
ATTN: DT-2, Wpns. & Sys. Division

Director
Defense Nuclear Agency
ATTN: STSI, Archives
ATTN: DDST
ATTN: STSP
3cy ATTN: STTL, Tech. Library
3cy ATTN: SPAS

Director of Defense Research & Engineering
ATTN: DD/S&SS
ATTN: AD/OS
ATTN: AD/DS

Commander
Field Command, Defense Nuclear Agency
ATTN: FCTMOF
ATTN: FCPR
ATTN: FCTMD

Director
Joint Strat. Tgt. Planning Staff, JCS
ATTN: JLTW-2
ATTN: JPTM
ATTN: JPTP

Chief
Livermore Division, Field Command, DNA
ATTN: FCPRL

OJCS/J-5
ATTN: J-5, Plans & Policy, R&D Division

DEPARTMENT OF THE ARMY

Program Manager
BMD Program Office
ATTN: DACS-BMZ
ATTN: DACS-BMT, John Shea
ATTN: DACS-BMZ-D, Julian Davidson
ATTN: DACS-BMT, Clifford E. McLain

Commander
BMD System Command
ATTN: BDMSC-TEN, Noah J. Hurst

DEPARTMENT OF THE ARMY (Continued)

Deputy Chief of Staff for Rsch. Dev. & Acq.
ATTN: NCB Division

Deputy Chief of Staff for Ops. & Plans
ATTN: Dir. of Chem. & Nuc. Ops.

Commander, Harry Diamond Laboratories
ATTN: DRXDO-RC, Robert B. Oswald, Jr.
ATTN: DRXDO-NP
ATTN: DRXDO-RBH, James H. Gwaltney

Commander
Picatinny Arsenal
ATTN: SMUPA-MD, Henry Opat
ATTN: SARPA-ND-C-T, Donald Miller
ATTN: SARPA-FR-E, Louis Avrami

Commander
TRASANA
ATTN: R. E. DeKinder, Jr.

Director
U.S. Army Ballistic Research Labs.
ATTN: Robert E. Eichelberger
ATTN: DRXBR-TB, J. T. Frasier
ATTN: DRXRD-BVL, William J. Schuman, Jr.

Commander
U.S. Army Mat. & Mechanics Rsch. Ctr.
ATTN: DRXMR-HH, John F. Dignam

Commander
U.S. Army Materiel Dev. & Readiness Cmd.
ATTN: DRCDE-D, Lawrence Flynn

Commander
U.S. Army Missile Command
ATTN: DRSMI-XS, Chief Scientist
ATTN: DRSMI-RRR, Bud Gibson
ATTN: DRS-RKP, W. B. Thomas
ATTN: DRCPM-PE-EA, Wallace O. Wagner

Commander
U.S. Army Nuclear Agency
ATTN: ATCA-NAW

DEPARTMENT OF THE NAVY

Chief of Naval Material
ATTN: Mat 0323, Irving Jaffee

Chief of Naval Operations
ATTN: OP 985D
ATTN: OP 62
ATTN: OP 985

Chief of Naval Research
ATTN: Code 464, Thomas P. Quinn

Director
Naval Research Laboratory
ATTN: Code 7770, Gerald Cooperstein
ATTN: Code 5180, Mario A. Persechino
ATTN: Code 2027, Tech. Library

DEPARTMENT OF THE NAVY (Continued)

Commander
Naval Sea Systems Command
ATTN: 0333A, Marlin A. Kinna

Commander
Naval Surface Weapons Center
ATTN: Code 323, W. Carson Lyons
ATTN: Code WA501, Navy Nuc. Prgms. Off.
ATTN: Code 2302, Leo F. Gowen

Director
Strategic Systems Project Office
ATTN: NSP-272, CDR Leslie Stoessl

DEPARTMENT OF THE AIR FORCE

AF Materials Laboratory, AFSC
ATTN: MAS
ATTN: MBC, Donald L. Schmidt
ATTN: T. Nicholas

AF Rocket Propulsion Laboratory, AFSC
ATTN: RTSN, G. A. Beale

AF Weapons Laboratory, AFSC
ATTN: SUL
ATTN: DYS, Lt E. J. Burns
ATTN: DYV
ATTN: Dr. Minge

Commander
Foreign Technology Division, AFSC
ATTN: TDFBD, J. D. Pumphrey
ATTN: TDPTN

HQ USAF/RD
ATTN: RDPM
ATTN: RDQ
ATTN: RDQSM
ATTN: RD
ATTN: RDQPN

SAMSO/DY
ATTN: DYS

SAMSO/MN
ATTN: MNMR

SAMSO/RS
ATTN: RSSE
ATTN: RSS

Commander in Chief
Strategic Air Command
ATTN: DOXT
ATTN: XPFS

ENERGY RESEARCH AND DEVELOPMENT ADMIN

Division of Military Application
ATTN: Doc. Con. for Res. & Dev. Branch
ATTN: Doc. Con. for CDR Richard E. Peterson
ATTN: Doc. Con. for LTC Donald L. McNutt

University of California
ATTN: C. Joseph Taylor, L-92
ATTN: Joseph E. Keller, Jr., L-125
ATTN: G. Staihle, L-24

ENERGY RESEARCH AND DEVELOPMENT ADMIN
(Continued)

Los Alamos Scientific Laboratory
ATTN: Doc. Con. for J. W. Taylor
ATTN: Doc. Con. for John McQueen
ATTN: Doc. Con. for R. S. Thurston

Sandia Laboratories
ATTN: Raymond Ng
ATTN: Doc. Con. for T. Gold
ATTN: Doc. Con. for C. S. Hoyle
ATTN: Doc. Con. for 8131, H. F. Norris, Jr.

Sandia Laboratories
ATTN: Doc. Con. for Albert Chabai
ATTN: Doc. Con. for R. R. Boade
ATTN: Doc. Con. for D. McCloskey

DEPARTMENT OF DEFENSE CONTRACTORS

Aeronautical Rsch. Assoc. of Princeton, Inc.
ATTN: Coleman Donaldson

Aeronutronic Ford Corporation
Aerospace & Communications Ops.
Aeronutronic Division
ATTN: P. Spangler

Aerospace Corporation
ATTN: W. Barry
ATTN: R. Allen
ATTN: Richard Crolius, A2-RM1027

Avco Research & Systems Group
ATTN: John Gilmore, J400
ATTN: John E. Stevens, J100

Battelle Memorial Institute
ATTN: Merwyn R. Vanderlind
ATTN: W. Pfeifer

The Boeing Company
ATTN: Brian Lempriere

Brown Engineering Company, Inc.
ATTN: Ronald Patrick

Effects Technology, Inc.
ATTN: Robert Wengler

General Electric Company
Space Division
ATTN: G. Harrison
ATTN: Carl Anderson
ATTN: Phillip Cline

General Electric Company
TEMPO-Center for Advanced Studies
ATTN: DASIAC

General Research Corporation
ATTN: Robert E. Rosenthal

Institute for Defense Analyses
ATTN: Joel Bengston
ATTN: IDA Librarian, Ruth S. Smith

Ion Physics Corporation
ATTN: Robert D. Evans

DEPARTMENT OF DEFENSE CONTRACTORS
(Continued)

Kaman Avidyne
Division of Kaman Sciences Corp.
ATTN: Norman P. Hobbs

Kaman Sciences Corporation
ATTN: Albert P. Bridges
ATTN: Thomas Meagher
ATTN: Frank H. Shelton
ATTN: Jerry L. Harper
ATTN: John R. Hoffman

Lockheed Missiles and Space Company
ATTN: A. P. Hardt
ATTN: Lloyd F. Chase
ATTN: Raymond R. Capiaux
ATTN: F. G. Borgardt

Martin Marietta Aerospace
ATTN: Laird Kinnaird

McDonnell Douglas Corporation
ATTN: L. Cohen
ATTN: J. Kirby
ATTN: J. F. Garibotti
ATTN: R. J. Reck

National Academy of Sciences
ATTN: National Materials Advisory Board for
Donald G. Groves

Northrop Corporation
ATTN: Don Hicks

Physics International Company
ATTN: Doc. Con. for James Shea

Prototype Development Associates, Inc.
ATTN: John Slaughter

DEPARTMENT OF DEFENSE CONTRACTORS
(Continued)

R & D Associates
ATTN: Albert L. Latter
ATTN: Jerry Carpenter
ATTN: Harold L. Brode
ATTN: F. A. Field

Science Applications, Inc.
ATTN: R. Fisher
ATTN: G. Ray

Science Applications, Inc.
ATTN: J. Courtney

Southern Research Institute
ATTN: C. D. Pears

Stanford Research Institute
ATTN: Donald Curran
ATTN: Herbert E. Lindberg
ATTN: George R. Abrahamson
ATTN: J. T. Rosenberg
ATTN: M. J. Ginsberg

Stanford Research Institute
ATTN: Harold Carey

Systems, Science and Software, Inc.
ATTN: G. A. Gurtman
ATTN: Russell E. Duff

Terra Tek, Inc.
ATTN: Sidney Green